



저작자표시-비영리-변경금지 2.0 대한민국

이용자는 아래의 조건을 따르는 경우에 한하여 자유롭게

- 이 저작물을 복제, 배포, 전송, 전시, 공연 및 방송할 수 있습니다.

다음과 같은 조건을 따라야 합니다:



저작자표시. 귀하는 원저작자를 표시하여야 합니다.



비영리. 귀하는 이 저작물을 영리 목적으로 이용할 수 없습니다.



변경금지. 귀하는 이 저작물을 개작, 변형 또는 가공할 수 없습니다.

- 귀하는, 이 저작물의 재이용이나 배포의 경우, 이 저작물에 적용된 이용허락조건을 명확하게 나타내어야 합니다.
- 저작권자로부터 별도의 허가를 받으면 이러한 조건들은 적용되지 않습니다.

저작권법에 따른 이용자의 권리는 위의 내용에 의하여 영향을 받지 않습니다.

이것은 [이용허락규약\(Legal Code\)](#)을 이해하기 쉽게 요약한 것입니다.

[Disclaimer](#)

이학석사 학위논문

Epitaxial Growth of Thin Film
Iron Chalcogenide FeSe
on SrTiO₃(100) and GaP(111)

철 칼코겐 화합물 FeSe 박막의 SrTiO₃(100)와
GaP(111) 위에서의 에피택시 성장

2017년 2월

서울대학교 대학원

물리천문학부 물리학전공

유용찬

Epitaxial Growth of Thin Film
Iron Chalcogenide FeSe
on SrTiO₃(100) and GaP(111)

지도교수 국 양

이 논문을 이학석사 학위논문으로 제출함
2017년 1월

서울대학교 대학원
물리천문학부 물리학전공
유용찬

유용찬의 이학석사 학위논문을 인준함
2017년 1월

위원장 _____ 김 대 식 (인)

부위원장 _____ 국 양 (인)

위 원 _____ 양 범 정 (인)

Abstract

Epitaxial Growth of Thin Film Iron Chalcogenide FeSe on SrTiO₃(100) and GaP(111)

Yong-Chan Yoo

Department of Physics and Astronomy, Physics Major

The Graduate School

Seoul National University

High-temperature superconductivity is one of the most important areas of research in condensed matter physics. In particular, iron-based high-temperature superconductors have a completely different Fermi level symmetry than BCS superconductors or copper-based superconductors, which have been used to form superconductors. Therefore, new physics is needed to explain the mechanism of this superconducting phenomenon. Among them, FeSe, which is an iron chalcogenide superconductor, is very valuable because it has a relatively simple structure and high superconducting transition temperature. This thesis deals with the thin film growth of these FeSe on SrTiO₃(100) and GaP(111) substrates. In this experiment, FeSe samples were grown on substrates using molecular beam epitaxy (MBE), in which Fe and Se were calibrated with a quartz crystal microbalance (QCM). The crystallinity of the growing sample was

confirmed by low energy electron diffraction (LEED) and high energy reflection electron diffraction (RHEED). The samples grown under various conditions were examined for their surface and electronic structure at low temperatures of liquid nitrogen and liquid helium through a scanning tunneling microscope (STM) and scanning tunneling spectroscopy (STS) without contamination inside the ultra-high vacuum chamber. The samples showed tetragonal structure on SrTiO₃(100) substrate and hexagonal structure on GaP (111) substrate. Various surface reconstructions of these structures at atomic level were also confirmed.

Keywords: Iron-Based Superconductor, Iron Chalcogenides, Thin Film, Molecular Beam Epitaxy, Scanning Tunneling Microscopy

Student Number: 2015-20339

Table of Contents

Chapter 1 Introduction.....	1
1.1 Overview of Superconductivity	1
1.2 Iron-Based Superconductor.....	6
1.3 Thin Film Iron-Based Superconductor FeSe	10
1.3.1 Crystal structure of FeSe.....	10
1.3.2 Recent studies of thin film iron-based superconductor FeSe.....	12
Chapter 2 Instrumentation	14
2.1 Principles of Instruments	14
2.1.1 Scanning Tunneling Microscopy (STM).....	14
2.1.2 Molecular Beam Epitaxy (MBE)	20
2.1.3 Low Energy Electron Diffraction (LEED).....	22
2.1.4 Reflection High Energy Electron Diffraction (RHEED)	23
2.2 STM-MBE Combined Systems.....	25
2.2.1 Variable low temperature STM-MBE combined system...25	
2.2.2 Low temperature STM-Laser-MBE combined system	27
Chapter 3 Epitaxial Growth of Thin Film FeSe	29
3.1 Calibration of MBE deposition rate.....	29
3.2 FeSe on SrTiO ₃ (100)	31

3.2.1	SrTiO ₃ (100) substrate preparation	31
3.2.2	Epitaxial growth of tetragonal phases of thin film FeSe on SrTiO ₃ (100)	34
3.2.3	Epitaxial growth of hexagonal phases of thin film FeSe on SrTiO ₃ (100)	40
3.3	FeSe on GaP(111)	42
3.3.1	GaP(111) substrate preparation.....	42
3.3.2	Epitaxial growth of thin film FeSe on GaP(111)	45
Bibliography		49
Appendix.....		52
Appendix A STM Tip Fabrication by Electrochemical Etching and Focused Ion Beam (FIB)		52
Appendix B Epitaxial Growth of Monolayer GeSe on Ge(111) ..		54

List of Figures

Figure 1.1	Pairing mechanisms of superconductors	5
Figure 1.2	Crystal structures of the iron-based superconductors	8
Figure 1.3	Schematic of the 2-D projected Brillouine zone of the FeAs-based superconductors	9
Figure 1.4	Two representative phases of FeSe	11
Figure 2.1	Schematic diagram of scanning tunneling microscopy	15
Figure 2.2	Schematic diagram of quantum tunneling model	16
Figure 2.3	Geometry of the STM tip and the sample	18
Figure 2.4	Schematic diagram of molecular beam epitaxy	21
Figure 2.5	Two types of evaporators	21
Figure 2.6	Schematic diagram of LEED	22
Figure 2.7	3-Dimensional analysis of RHEED.....	24
Figure 2.8	Variable low temperature STM-MBE combined system	26
Figure 2.9	Low temperature STM-Laser-MBE combined system	28
Figure 3.1	SrTiO ₃ (100) substrate	33
Figure 3.2	FeSe on SrTiO ₃ (100)	35
Figure 3.3	Large area STM image of 10ML of FeSe on SrTiO ₃ (100) grew at 450°C	35
Figure 3.4	STM images of 10ML of FeSe on SrTiO ₃ (100) grew at 450°C ..	36
Figure 3.5	STM images of 10ML of FeSe on SrTiO ₃ (100) grew at various temperatures.....	37
Figure 3.6	STM images of various ratios of FeSe on SrTiO ₃ (100) grew at 450°C	38

Figure 3.7 STM image of FeSe on SrTiO ₃ (100) grew at 450°C at atomic resolution	39
Figure 3.8 STM images of hexagonal phase FeSe on SrTiO ₃ (100)	41
Figure 3.9 STM image of hexagonal phase FeSe on SrTiO ₃ (100) at atomic resolution	41
Figure 3.10 GaP(111) substrate.....	44
Figure 3.11 STM images of GaP(111) substrate.....	45
Figure 3.12 LEED patterns at 60V of Se etched GaP(111) and FeSe on GaP(111)	47
Figure 3.13 Schematic of the 2-D projected Brillouine zone of the FeAs-based superconductors	47
Figure 3.14 Schematic of the 2-D projected Brillouine zone of the FeAs-based superconductors	48
Figure A.1 SEM images of iridium STM tip.....	53
Figure B.1 STM image of monolayer GeSe on Ge(111)	56
Figure B.2 STM images of multilayer GeSe on Ge(111)	56
Figure B.3 Crystal structure of monolayer GeSe on Ge(111)	57
Figure B.4 Heterojunction between monolayer GeSe on Ge(111) and Ge(111) substrate	58
Figure B.5 IETS spectra of monolayer GeSe on Ge(111)	59

Chapter 1

Introduction

1.1 Overview of Superconductivity

Superconductivity is known as one of the most important fields of research in condensed matter physics because of its theoretical importance of the phenomenon itself and its practical value as a cornerstone of future technology. The superconducting phenomenon is represented by the fact that the DC resistance of the material is zero and the magnetic flux is expelled out from the material. This phenomenon of superconductivity was first discovered in 1911 by the Dutch physicist Kamerlingh Onnes [1]. Onnes was awarded the Nobel Prize for Physics in 1913 for his discovery that the electrical resistance of mercury was zero at 4.19K in his liquid helium experiments. Before long, it was discovered that other elemental materials such as lead and niobium show superconductivity at a low temperature of 10K or less, a new physics was needed to explain this phenomenon gradually.

The starting point of the theoretical understanding of superconductivity was based on various phenomenological understanding of superconductors. In 1935, German physicists Fritz London and Heinz London proposed the following two London equations [2].

$$\frac{\partial \mathbf{j}_s}{\partial t} = \frac{n_s e^2}{m} \mathbf{E} \quad (1.1)$$

$$\nabla \times \mathbf{j}_s = -\frac{n_s e^2}{mc} \mathbf{B} \quad (1.2)$$

The London penetration depth can be obtained by equating the second equation and the Ampere's law.

$$\nabla^2 \mathbf{B} = \frac{1}{\lambda^2} \mathbf{B}, \lambda = \sqrt{\frac{mc^2}{4\pi n_s e^2}} \quad (1.3)$$

Under the condition expressed by the London penetration depth, the electromagnetic free energy inside the superconductor is minimized. From this, the London brothers succeeded in describing the Meissner–Ochsenfeld effect in which the magnetic flux in the superconductor becomes zero.

Another theoretical milestone was established in 1950 by Vitali Ginzburg and Lev Davidovich Landau, both of them awarded the Nobel Prize for Physics in 2003 and 1962, respectively. The Ginzburg–Landau theory is based on a phenomenological explanation. They assumed the following Ginzburg–Landau free energy [3].

$$F = \int d^3x \left[\alpha |\psi|^2 + \frac{\beta}{2} |\psi|^4 + \gamma \left| \left(\nabla + \frac{2ie}{\hbar c} \mathbf{A} \right) \psi \right|^2 + \frac{B^2}{8\pi} \right] \quad (1.4)$$

They suggested that the phase transition between the normal state and the superconducting state occurs under the condition that the above Ginzburg–Landau free energy is minimized. This is expressed by the following equations.

$$\alpha \psi + \frac{\beta}{2} |\psi|^2 \psi - \gamma \left(\nabla + \frac{2ie}{\hbar c} \mathbf{A} \right)^2 \psi = 0 \quad (1.5)$$

$$\nabla \times \mathbf{B} = \frac{4\pi}{c} \mathbf{j}_s, \mathbf{j}_s = -\frac{4e}{\hbar} \gamma |\psi|^2 \left(\nabla V + \frac{2e}{\hbar c} \mathbf{A} \right) \quad (1.6)$$

From Ginzburg–Landau theory, superconductors can be divided into two classes: Type-I superconductor with first-order phase transition from normal and superconducting states at critical field B_c ; Type-II superconductor with a mixed state between two critical field B_{c1} and B_{c2} .

In 1957, John Bardeen, Leon N. Cooper, and John Robert Schrieffer came up with the first hypothesis to explain the microscopic interpretation of superconductivity. This is the famous BCS theory [4] [5]. The three men above were awarded the 1972 Nobel Prize for Physics for their achievements. According to BCS theory, two electrons with spin and momentum opposite to each other in a superconductor form a Cooper pair, acting like a bosonic particle, mediated by phonons in the lattice [6]. The mean-field BCS Hamiltonian and the BCS ground state of BCS superconductors expressed by the second quantization formalism is as follows.

$$H_{\text{BCS}} = \sum_{\mathbf{k}, \sigma} \varepsilon_{\mathbf{k}} n_{\mathbf{k}, \sigma} + \sum_{\mathbf{k}, \mathbf{l}} V_{\mathbf{k}, \mathbf{l}} c_{\mathbf{k}, \uparrow}^{\dagger} c_{-\mathbf{k}, \downarrow}^{\dagger} c_{-\mathbf{l}, \uparrow} c_{\mathbf{l}, \uparrow} \quad (1.7)$$

$$|\text{BCS}\rangle_G = \prod_{\mathbf{k}} (u_{\mathbf{k}} + v_{\mathbf{k}} c_{\mathbf{k}, \uparrow}^{\dagger} c_{-\mathbf{k}, \downarrow}^{\dagger}) |0\rangle \quad (1.8)$$

The above BCS ground state can be easily described by using the new operators that transformed from the original operators through the Bogoliubov transformation [7]. The Bogoliubov transformation is generally a linear transformation and can be written as:

$$\alpha_{\mathbf{k}, \sigma} = u_{\mathbf{k}} c_{\mathbf{k}, s} - \sigma v_{\mathbf{k}} c_{-\mathbf{k}, -\sigma}^{\dagger} \quad (1.9)$$

Diagonalizing the BCS Hamiltonian with the transformed basis and placing

a new parameter $\Delta_{\mathbf{k}} = \sum_{\mathbf{l}} V_{\mathbf{k},\mathbf{l}} \mu_{\mathbf{l}} v_{\mathbf{l}}^*$, the gap equation of the BCS superconductor can be derived as follows.

$$\Delta_{\mathbf{k}} = -\frac{1}{2} \sum_{\mathbf{l}} V_{\mathbf{k},\mathbf{l}} \frac{|\Delta_{\mathbf{l}}|}{\sqrt{(\varepsilon_{\mathbf{k}} - \mu)^2 + |\Delta_{\mathbf{k}}|^2}} \quad (1.10)$$

The superconducting transition temperature (T_c) can be obtained from the gap equation obtained by the microscopic theory.

According to BCS theory, superconductors with T_c above 30K cannot exist. However, this belief was broken in 1986 when Georg Bednorz and Alex Müller discovered that the cuprate material lanthanum barium copper oxide, so called LBCO, had a T_c of 35K [8]. Soon after, it was observed that another cuprate material YBaCuO had a T_c of 92K [9], and research on high-temperature (high- T_c) superconductors began. These high- T_c superconductors are a totally new kind of physical property that cannot be explained by the existing BCS theory. high- T_c superconductors are sometimes referred to as unconventional superconductors, especially because the pairing mechanism of electrons is different from that described in the BCS theory. The following Figure 1.1 represents a schematic diagram showing the electron pairing mechanism in BCS superconductors and unconventional superconductors. Meanwhile, the two men who pioneered these fields were awarded the Nobel Prize for Physics in 1987. Subsequently, high- T_c superconductors based on copper such as BSCCO [10] and TBCCO [11] were continuously discovered. In 2008, a new type of iron-

based high- T_c superconductor, $\text{LaO}_{1-x}\text{F}_x\text{FeAs}$, was discovered [12]. As will be discussed in more detail later, new iron-based superconductors were subsequently discovered. Until now, a new type of high- T_c superconductor is still being discovered.

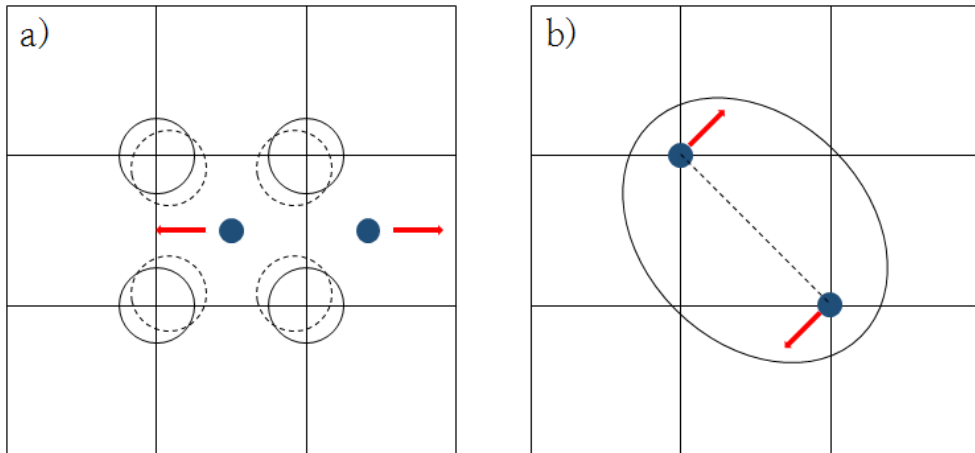


Figure 1.1: Pairing mechanisms of superconductors. a) In conventional superconductors, electron pairs are mediated by attractive interactions caused by phonons. b) In unconventional superconductors, electron pairs are created by their relative motion caused by spatial anisotropy.

1.2 Iron-Based Superconductor

As mentioned in the previous chapter, the first iron-based high- T_c superconductor $\text{LaO}_{1-x}\text{F}_x\text{FeAs}$ was discovered in 2008, boosting interest in another iron-based high- T_c superconductor. Most of the iron-based superconductors known to date are divided into four types as '1111', '122', '111', and '11' based on the ratio of elements and crystal structure as shown in Figure 1.2 [13]. Among these, iron-based superconductors belonging to the '1111', '122' and '111' parent material, which are mainly composed of iron pnictide compounds, are composed of two different layered structures. One is a layer of FeP or FeAs, known as in which superconductivity strongly occurs in the compounds, and the other is rare-earth oxide or fluoride such as LaO or SrF, known as a 'blocking layer', which acts as charge reservoir. These two layers alternate and form the overall crystal structure of iron pnictide superconductors. Unlike these materials, iron-based superconductors belonging to the '11' family are dominated by iron chalcogenides. These have a simple stack structure of repeating FeSe or FeTe layers in which there is no double stack structure like that of the iron pnictide compounds.

Iron-based superconductors have significantly different electronic structures than other superconductors. The electron density near the Fermi level of these iron-based superconductors is contributed mostly by in bonds made by iron pnictide or iron chalcogenide compounds. In particular, the complexity of the d-orbitals possessed by iron creates a multiband system of

these iron-based superconductors. The multiple bands of holes and electrons in iron-based superconductors have a specific symmetry on the Fermi surface, which is very important to reveal the electron pairing mechanism of these kinds of materials. However, the very complicated orbital structure of iron-based superconductors and the subtle differences in energy levels make it difficult to identify the mechanisms of superconducting phenomena. To date, the candidates for the electron pairing mechanism in iron-based superconductors have been thought of as spin density waves (SDW) and charge density waves (CDW) in addition to the electron-phonon interaction discussed in conventional BCS superconductors. Particularly, SDW requires more theoretical considerations in that it is based on repulsive potential, unlike the other two candidates [14]. Figure 1.3 shows the three representative pairing symmetries in 2-D Brillouin regions that iron-based superconductors are likely to have.

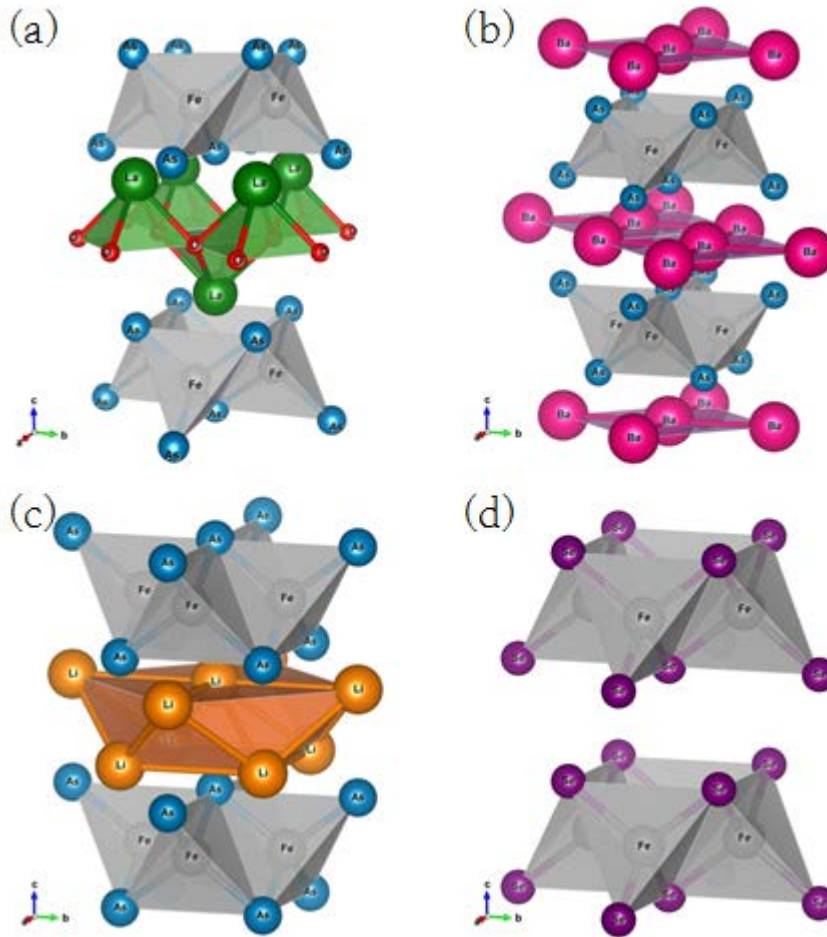


Figure 1.2: Crystal Structures of the iron-based superconductors. All superconductors have a tetragonal crystal structure, which are drawn by VESTA [15]. Atomic positions are determined by the Wickoff positions. **(a)** ‘1111’ superconductor LaOFeAs ($P4/nmm$). **(b)** ‘122’ superconductor BaFe_2As_2 ($I4/mmm$). **(c)** ‘111’ superconductor LiFeAs ($P4/nmm$). **(d)** ‘11’ superconductor FeSe ($P4/nmm$).

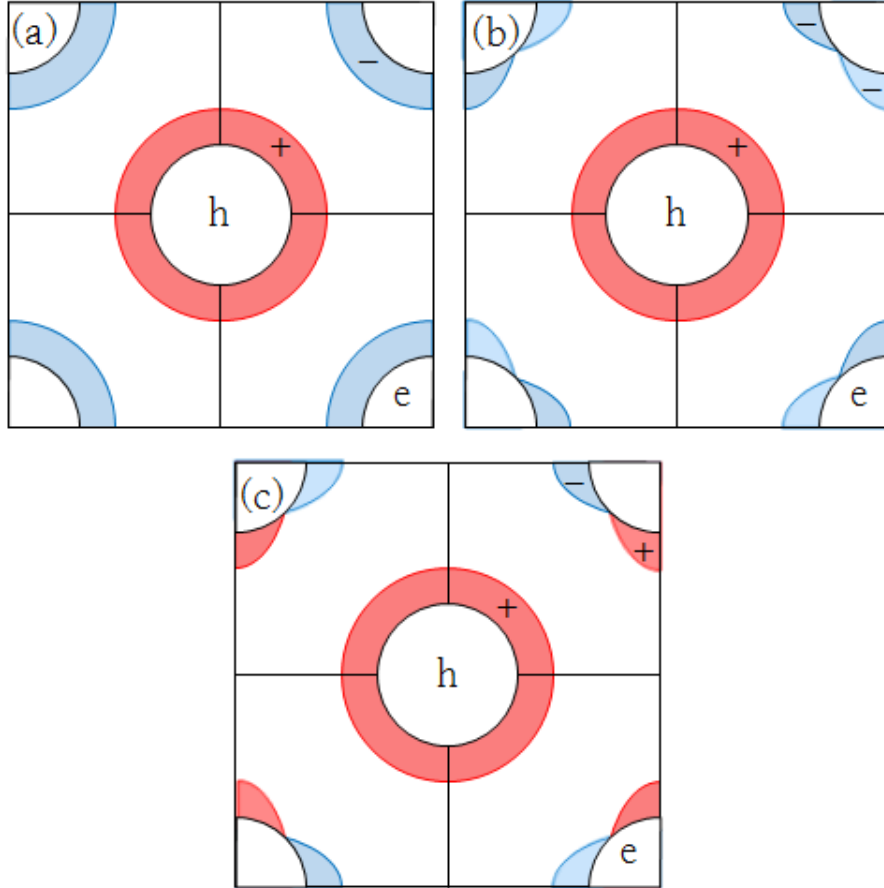


Figure 1.3: Schematic of the 2-D projected Brillouin zone of the FeAs-based superconductors. In this projection, the multiple bands of the system reduced to single hole (h, red shaded region) and electron (e, blue shaded region) pockets. (a) s-wave symmetry. (b) s-wave symmetry with anisotropy. (c) d-wave symmetry.

1.3 Thin Film Iron–Based Superconductor FeSe

Bulk and thin film iron–based superconductors may exhibit different behaviors. Especially, thin film iron–based superconductors are expected to play a very important role in the development of next generation devices such as superconducting junction, SQUID, wire and tape due to their high superconducting transition temperature and low anisotropy [16].

1.3.1 Crystal structure of FeSe

FeSe is a substance belonging to the iron chalcogenide compound of the '11' series categorized above. As shown in Figure 1.4, FeSe has several different crystal structures. Among these, the structure of FeSe classified as '11' iron–based superconductor is in Figure 1.4 (a), so called PbO type or alpha phase structure. This structure, which is classified as a tetragonal lattice, has $P4/nmm$ symmetry in space group. More specifically, iron atoms are arranged in a square lattice and selenium atoms form another square lattice at each center of the iron square lattice, intersecting up and down the height. Figure 1.4 (b) is called NiAs structure or beta phase. The beta phase is the hexagonal lattice with the $P63/mmc$ symmetry in the space group, not the tetragonal lattice. Unfortunately, superconductivity has not been reported in these hexagonal lattices so far. In addition, there are many phases, such as $FeSe_x$, with different composition ratios of Fe and Se [17]. Also, whether superconducting phenomena exist in these structures has not

yet been clarified.

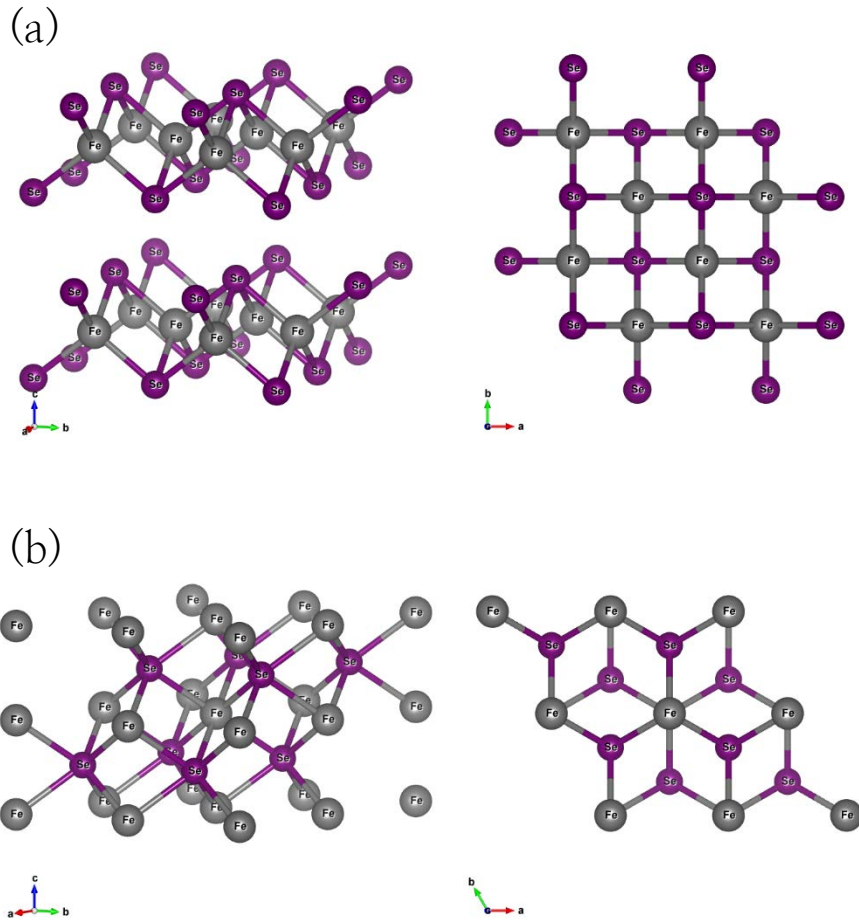


Figure 1.4: Two representative phases of FeSe. (a) PbO type (α -phase) FeSe with tetragonal symmetry. (b) NiAs type (β -phase) FeSe with hexagonal symmetry.

1.3.2 Recent studies of thin film iron-based superconductor FeSe

Since 2008, when iron-based superconductors first appeared, iron-based superconductors with higher T_c have continued to emerge. However, the discovery of iron-based superconductors with a T_c above 55K was not easy. Thin film iron-based superconductor FeSe began to attract a great deal of attention as it was known to have a T_c several times higher than the bulk FeSe [18]. In 2012, the discovery of single layer of FeSe grown on the SrTiO₃ substrate (FeSe/STO), which has T_c near 65K, began accelerating the study of iron-based high- T_c superconductors [19]. Especially in 2014, single layer of FeSe/STO has a T_c over 100K [20]. In subsequent experiments, it was also discovered that FeSe/STO has *s*-wave symmetry by analyzing the STM / STS and QPI pattern analysis. The relationship between structural symmetry, magnetic ordering and superconducting mechanism is also actively being carried out [21]. Despite many efforts, the exact mechanism of the extraordinarily high T_c of FeSe/STO has not been clarified until now. Although there are some conjectures, the theory that the electron-phonon interaction at the interface between the STO and the FeSe has been greatly activated and thus has such a property is convincingly accepted [22]. In order to verify these theories, further studies on phonon energy is required through experiments such as using isotopes or changing strain between the interfaces.

As a result of the interface effect between STO and FeSe, the research on the interface between the superconducting thin film and the

superconducting thin film or between the superconducting thin film and the other material has started recently. In 2014, as the topological state and the superconducting state are discovered simultaneously in the single layer of FeSe, interest in new physics arising from the combination of these materials is increasing [23]. The research on iron-based thin-film superconductor FeSe is expected to be in the future as it is related to practical aspects as well as research on the new state of matter.

Chapter 2

Instrumentation

2.1 Principles of Instruments

2.1.1 Scanning Tunneling Microscopy (STM)

In recent research in quantum physics, special types of experimental instrument are required to meet the characteristics of each subject because of the complexity of the sample to be studied. In particular, various types of scanning probe microscopes (SPM) have been used to observe local properties of the sample. Scanning tunneling microscopy (STM) was first developed by Gerd Binnig and Heinrich Rohrer in 1981 as an aid to this scanning probe microscope [24]. Since STM has been able to observe the surface and electronic structure of materials at atomic resolution, it has been a powerful experimental instrument. The two men were awarded the 1986 Nobel Prize for Physics for this achievement.

STM is an experimental instrument that utilizes the phenomenon of quantum tunneling as its name implies. Figure 2.1 is a schematic diagram of STM. Basically, the STM measures the tunneling current flowing between a metal tip with an apex of several tens of nanometers and a sample. By adjusting the magnitude of the tunneling current flowing between the tip and the sample by the feedback circuit, the distance between the tip and the sample can be adjusted to several angstroms or less. This microscopic

movement of the STM tip can be realized by a ceramic scanner with piezoelectricity.

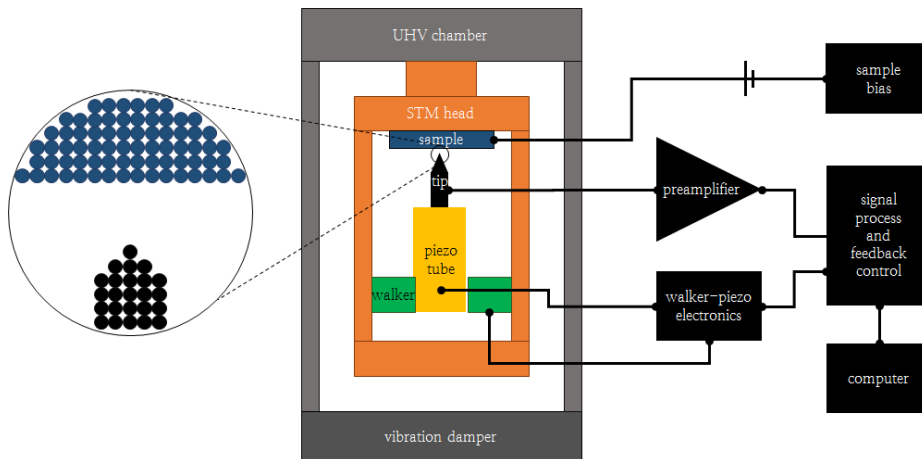


Figure 2.1: Schematic diagram of scanning tunneling microscopy.

The quantum tunneling phenomenon, which is the basic principle of STM, can be seen in a little more. In general, electrons present at the Fermi level of a metal-like sample become free electrons when they receive energy as much as the work function ϕ . When the STM tip is brought close to the sample at the tunneling regime, the electron tunneling phenomenon occurs between the tip and the sample by overcoming the work function ϕ . If the bias voltage V is applied as shown in Figure 2.2, the Fermi level of the tip becomes lower by eV relative to the Fermi level of the sample. As a result, tunneling occurs in which the electrons of the sample fill the empty state of the tip, creating a net tunneling current between the two.

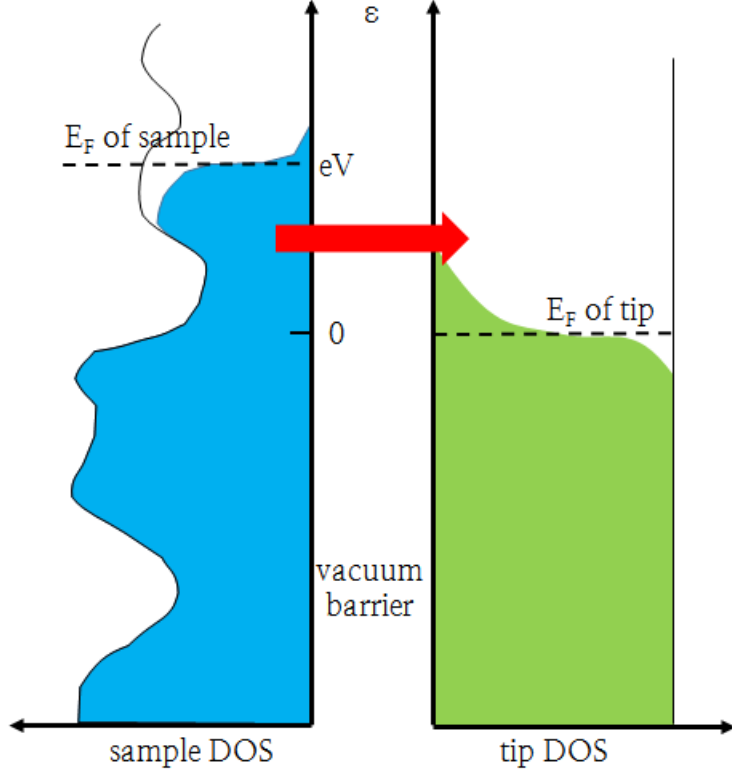


Figure 2.2: Schematic diagram of quantum tunneling model.

The following Bardeen's tunneling formula represents this tunneling current more precisely [25].

$$I = \frac{4\pi e}{\hbar} \int_0^{eV} d\varepsilon |M|^2 \rho_s(\varepsilon) \rho_t(\varepsilon - eV) \quad (2.1)$$

Here, $|M|^2$ is the tunneling matrix element, $\rho_s(\varepsilon)$ and $\rho_t(\varepsilon)$ are the density of states (DOS) of the sample and tip, respectively. The tunneling matrix element can be expressed again as:

$$M_{\mu\nu} = \frac{\hbar^2}{2m} \int dS (\psi_\mu^* \nabla \psi_\nu - \psi_\nu \nabla \psi_\mu^*) \quad (2.2)$$

For a typical metal–vacuum–metal junction, the tunneling current for the s–wave tip is proportional to the tunneling probability at the junction. There is

a well-known exponential decaying factor in this proportional relationship.

$$P \propto |\psi(0)|^2 e^{-2\kappa d} \quad (2.3)$$

$$\kappa = \frac{\sqrt{2m\phi}}{\hbar} \quad (2.4)$$

On the other hand, from the two equations for the tunneling matrix element $|M|^2$, it is clear that $|M|^2$ is proportional to the tunneling probability. Using this, it can be expressed as $|M|^2 = e^{-2\kappa d}$ and thus the tunneling current can be rewritten as:

$$I = \frac{4\pi e}{\hbar} \exp\left(-\frac{\sqrt{8m\phi}}{\hbar} d\right) \rho_t(0) \int_0^{eV} d\varepsilon \rho_s(\varepsilon) \quad (2.5)$$

In this calculation, it is assumed that the tip's DOS is constant in the tunneling domain.

Meanwhile, Gerd Binnig and Heinrich Rohrer presented a simple argument to determine the lateral resolution of the STM. Figure 2.3 shows the tip and sample geometry presented by this argument. In this case, the lateral distribution of the tunneling current is as follows [26].

$$I(\Delta x) = I_0 \exp\left(-2\kappa \frac{\Delta x^2}{2R}\right) \quad (2.6)$$

Typically, $\kappa \approx 1 \text{ \AA}^{-1}$. For $R = 100 \text{ \AA}$ and $\Delta x = 15 \text{ \AA}$, the current drops by a factor of $e^{-2} \approx 1/10$. However, the actual resolution is obtained below this value due to the atomic orbital and local variation of sample surface.

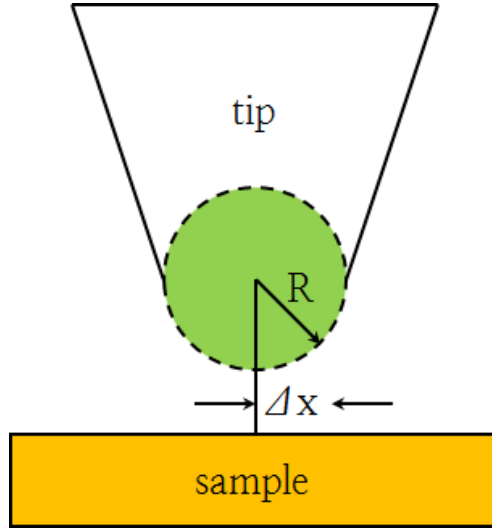


Figure 2.3: Geometry of the STM tip and the sample.

The STM maintains a constant tunneling current by a feedback circuit during the scanning process to obtain the topography of the surface of the sample. According to the Bardeen's tunneling formula described above, a constant value of the tunneling current means a constant value of the DOS integral. From this proportional relationship, the DOS at each bias of the sample can be obtained.

$$\frac{dI}{dV} = \frac{4\pi e}{\hbar} \exp\left(-\frac{\sqrt{8m\phi}}{\hbar} d\right) \rho_t(0) \rho_s(eV) \quad (2.7)$$

The above equation is a derivative of Bardeen's tunneling formula with bias voltage. This has a value proportional to DOS at each bias of the sample. Therefore, the DOS of the sample can be obtained by differentiating the relationship between the measured tunneling current and the bias voltage.

With the lock-in amplifier, the DOS of the sample can be obtained more precisely. This concept can be achieved by adding a small modulation voltage to the bias voltage as shown below.

$$V = V_0 + V_{\text{mod}} \sin(\omega t) \quad (2.8)$$

Therefore, the modulated tunneling current can be expressed as follows.

$$I(V) = I(V_0) + \left. \frac{dI}{dV} \right|_{V_0} V_{\text{mod}} \sin(\omega t) + \frac{1}{2} \left. \frac{d^2 I}{dV^2} \right|_{V_0} V_{\text{mod}}^2 \sin^2(\omega t) + \dots \quad (2.9)$$

A closer examination reveals that the first and the second harmonic frequency are proportional to dI/dV and d^2I/dV^2 , respectively. From this, the DOS and inelastic spectrum at each bias of the sample can be obtained.

2.1.2 Molecular Beam Epitaxy (MBE)

Molecular beam epitaxy (MBE), first developed by John Arthur and Alfred Cho in the late 1960s, is a method of epitaxially growing thin films by depositing atomic or molecular-level beams on the surface of a sample [27]. Figure 2.4 is a schematic diagram of MBE.

MBE is a method that is required for very precise and clean sample growth and is basically used in UHVs below 10^{-8} torr. In addition to the UHV chamber, there are evaporators, tools for depositing ingredient materials of the sample to be grown by heating them at the appropriate temperature, as a part of the MBE. The atomic or molecular beam emitted from this evaporator is deposited on the surface of the substrate with sufficient temperature and reacted to grow the desired sample. The sample usually grows to less than 1 nm per second and forms an epitaxial thin film. This low growth rate not only allows the thin film to determine its thickness at the monolayer level, but also allows the growth of compounds of very complex composition. In this experiment, two types of evaporator were used. The following Figure 2.5 is schematic view of the both types of MBE evaporator. One is crucible type evaporator for Se deposition, and the other is e-beam type evaporator for Fe deposition. A feedback circuit is usually available when you want a deposition rate at a precise level. In the above evaporators, the amount of flux was controlled through the shutter adjustment and the hole size of the shield.

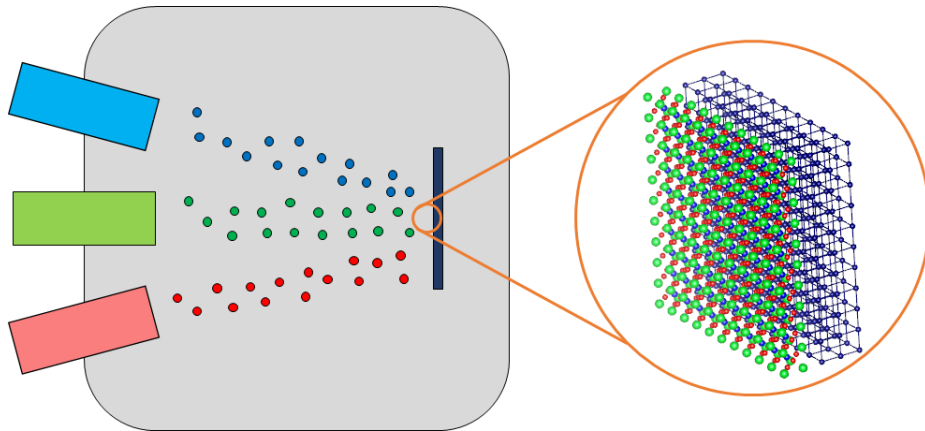


Figure 2.4: Schematic diagram of molecular beam epitaxy.

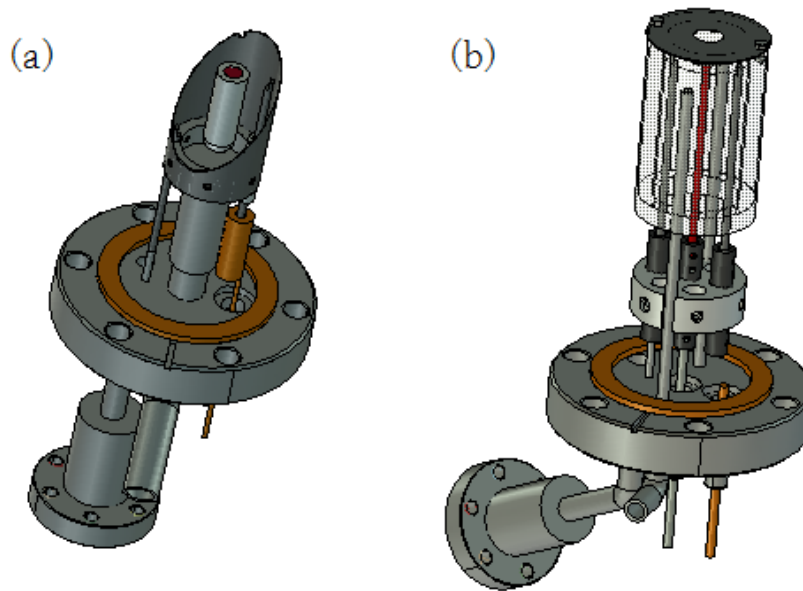


Figure 2.5: Two types of evaporators. (a) Crucible type Se evaporator for low temperature deposition. A standard Knudsen cell is used. (b) E-beam type Fe evaporator for high temperature deposition.

2.1.3 Low Energy Electron Diffraction (LEED)

Low Energy Electron Diffraction (LEED) is one of the methods of determining the crystal structure of a surface by diffracting electrons. Figure 2.6 shows a simplified representation of the structure of LEED. Usually, low energy electrons of 20 to 200 eV incident perpendicularly on the sample. These low-energy electrons have a wavelength of about several Å and are therefore suitable for determining the lattice structure of a solid material in general. Generally, the diffraction condition satisfies the Bragg condition and produces a LEED pattern on the screen for back-scattered electron beams that cause constructive interferences. Here, the LEED pattern on the screen corresponds to the reciprocal lattice of the surface lattice structure. Therefore, as the incident electron beam of high energy is used, the overall LEED pattern appears to converge toward the center. Also, peaks corresponding to a longer-range order appear closer to the center.

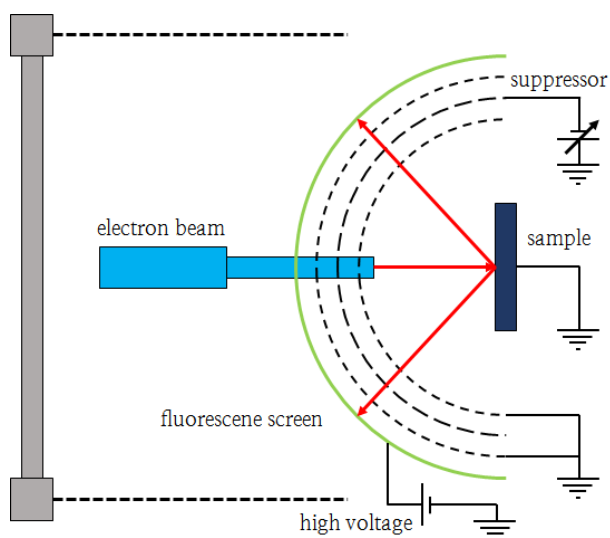


Figure 2.6: Schematic diagram of LEED.

2.1.4 Reflection High Energy Electron Diffraction (RHEED)

Reflection High Energy Electron Diffraction (RHEED) is widely used with LEED to understand the crystal structure of the sample surface. Figure 2.7 depicts the basic principles of RHEED in three dimensional space. RHEED is basically similar to LEED in that it uses electron diffraction patterns but uses higher energy electrons of 5 to 100 keV to utilize a forward-scattered electron beam. RHEED observes the interference patterns appearing on the screen by reflecting the electron beam of high energy incident on the surface of the sample almost in parallel at less than 5 degrees. Electron beams incident on the surface in parallel determine the crystal structure by passing through a large number of lattices along the surface. At the same time, since the momentum of the component perpendicular to the surface is small, it is suitable for examining the crystal structure of the surface with a resolution below the monolayer. Meanwhile, since the electron beams reflected from the surface of the sample have the same energy in the case of the elastic scattering, the momentum of these electrons exists on the same Ewald sphere. The reciprocal lattice of a 2-dimensional sample appears as a rod in three dimensional, where the constructive interference occurs at the point where the rod and Ewald sphere meet. Since RHEED is incident on the sample surface in parallel as described above, it is very advantageous to measure the structure of the growing sample *in-situ* compared to other equipment. Therefore, monitoring the growth of thin films using both RHEED and MBE is a widely used technique.

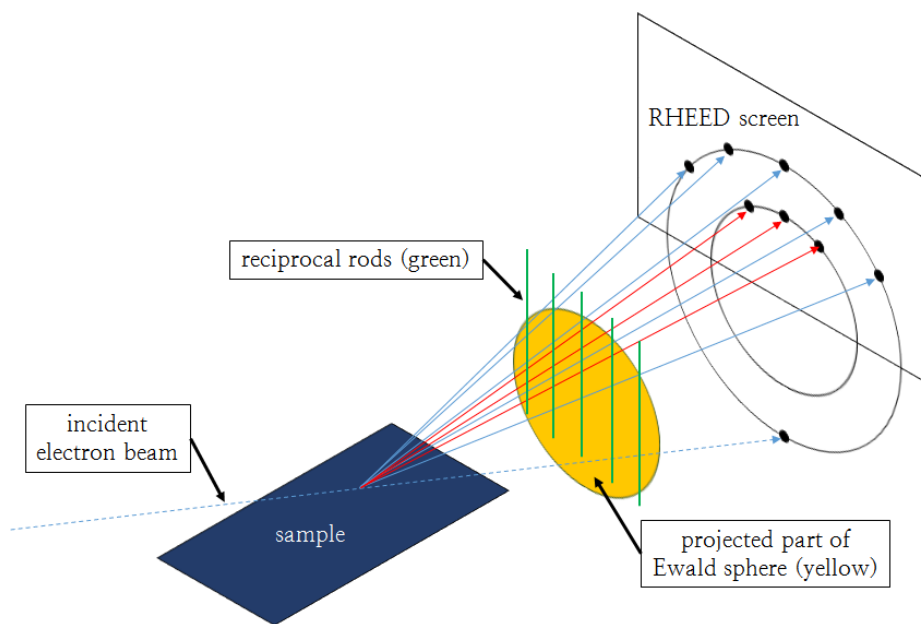


Figure 2.7: 3-Dimensional analysis of RHEED.

2.2 STM–MBE Combined System

For this experiment, two STM–MBE combined systems were involved. The STM–MBE combined system is very powerful because it can study the surface of a material grown in atomic or molecular precise using MBE without contamination of the sample. In addition, by studying the structural and electronic properties of materials using STM, more detailed information on the growth of materials using MBE can be obtained. Due to these characteristics, research on the complex emergent quantum phenomena can be possible with using the STM–MBE combined system [28].

2.2.1 Variable low temperature STM–MBE combined system

The following Figure 2.8 is the whole structure of the first STM–MBE combined system used in the experiment. This system is a home–built system and consists of two chambers. The main chamber is containing the STM head and cryostats. The STM head is ‘Pan Type’ and designed to replace the STM tip for STM / STS experiments and the Micro four point probe (M4PP) for resistivity measurement on the surface of the sample. The head is also capable of low–temperature experiments at 79 K and 5.8 K, using liquid nitrogen and liquid helium respectively, through continuous flow of them. The system is equipped with a temperature controller (Lakeshore 332 Temperature Controller) to maintain a constant temperature above 60K under liquid nitrogen conditions and over 100K under liquid

helium conditions. On the other hand, XY and Z piezo scanners were calibrated with FeSe and Au (111), respectively. At liquid nitrogen temperature, the XY piezo has a range of 10 nm/V and the Z piezo has a range of 0.95 nm/V. Another chamber is a preparation chamber, in which a sample is grown using MBE. There are also external ports for installing the two evaporators mentioned above and sample heaters that allow the sample to be maintained at the proper growth temperature. Both chambers were maintained under UHV conditions which are lower than 1.0×10^{-10} torr. The prepared sample travels between the two chambers through a magnetic translator. In addition, samples and tips can be loaded into the system using a load-lock chamber connected to the preparation chamber.

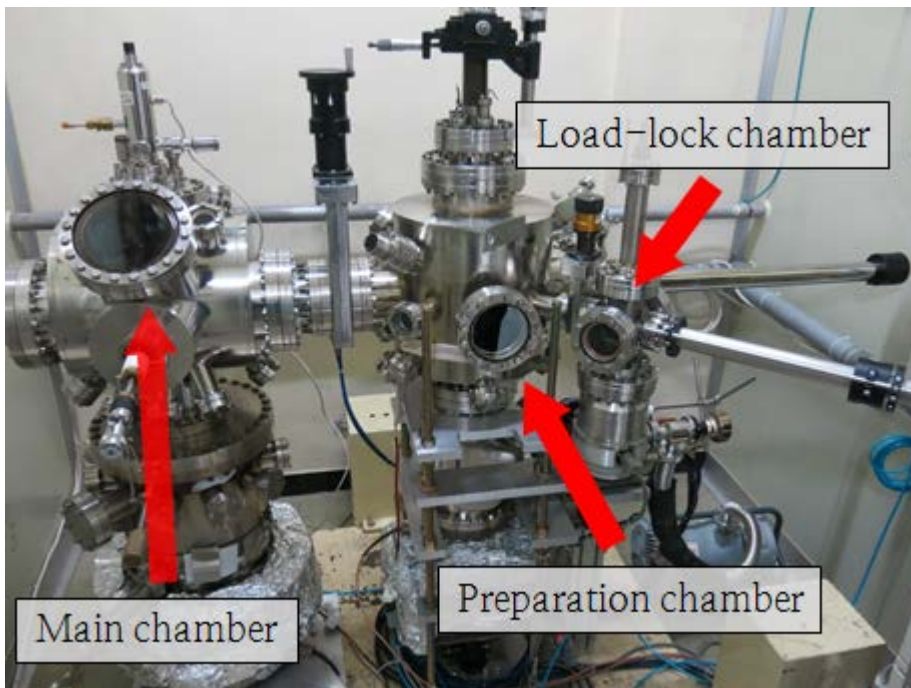


Figure 2.8: Variable low temperature STM-MBE combined system.

2.2.2 Low temperature STM–Laser–MBE combined system

Another system used in the experiment is the STM–Laser–MBE combined system. Figure 2.9 below shows the structure of this system. This system, which is also a home–built instrument, is divided into three parts. First, there is a main chamber with head and cryostats. This system uses a Pan Type walker head, and the cooling mechanism is the same as in the previous system. The XY and Z piezo scanners were calibrated using Si (111) and Au (111), respectively, and temperatures in liquid nitrogen and liquid helium could reach 79K and 8.0K, respectively. The second chamber is the preparation chamber, which serves as a station for heating and preserving samples and tips. The final third chamber is the MBE–PLD (Pulsed Laser Deposition) chamber where samples are grown in this chamber. The sample stage installed in the center of the chamber was designed to load and heat the sample. Two types of evaporators are installed through the bottom ports and an additional PLD is installed. In this system, PLD was mainly used to grow iron–based compounds of '111' or '122' series and was not used in this experiment. On the other hand, LEED and RHEED are also installed in the MBE–PLD chamber so that the growth of the sample can be confirmed in real time or as soon as it grows. Same as above, the sample can be moved to each chamber according to the purpose through magnetic translators. As with the above systems, all chambers were maintained in UHV conditions. Especially, the load–lock chamber of this system is connected to the vacuum chamber at the same time as the preparation chamber, so that the sample can be moved to another system while maintaining the UHV condition.

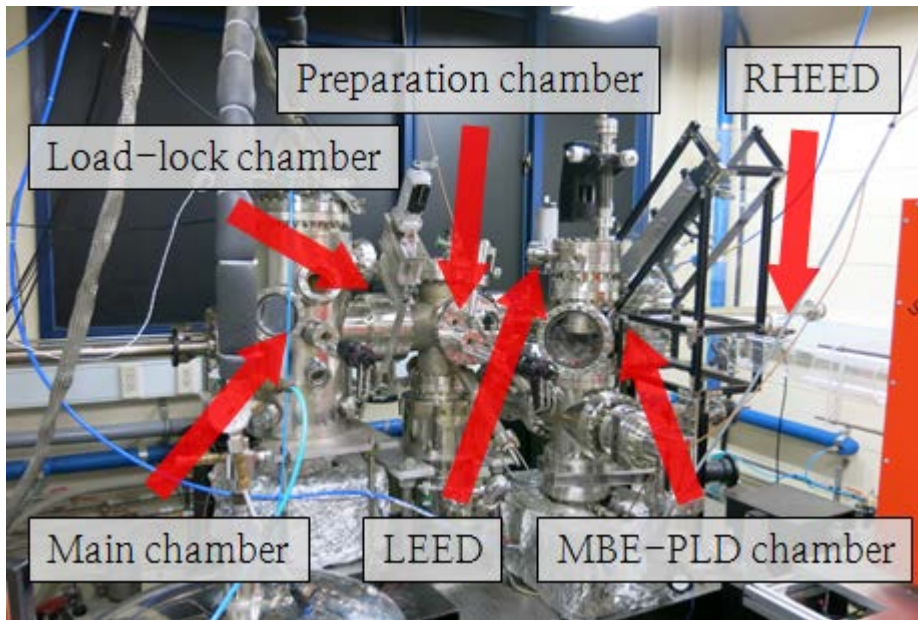


Figure 2.9: Low temperature STM-Laser-MBE combined system.

Chapter 3

Epitaxial Growth of Thin Film FeSe

3.1 Calibration of MBE deposition rate

The main goal of this experiment was to grow thin films of FeSe on the two substrates SrTiO₃(100) and GaP(111) using MBE. The deposition of Fe and Se was performed using the e-beam type evaporator and the crucible type evaporator introduced in the previous chapter, respectively. In general, the growth of the thin film FeSe is affected by the crystal structure and temperature of the substrate. When the specific atom is substituted in the crystal structure of the substrate by some processes, the overall property of the interface may be largely changed. In particular, it is recently known that the superconductivity of thin film changes greatly depending on its own thickness. Therefore, controlling this thickness is a very important factor in thin film growth, and it is especially vital to calibrate the deposition rate accurately.

In this experiment, the INFICON QCM sensor and home-made QCM sensor with INFICON quartz crystal were used. In order to calibrate the deposition rate, the INFICON thickness monitor XTM/2 was also used. To analyze the sample growth conditions as quantitatively as possible, a QCM sensor was installed at the position where the actual sample was deposited. The INFICON QCM sensor was fixedly installed in the low

temperature STM–Laser–MBE combined system to measure the deposition rate. In the variable low temperature STM–MBE combined system, a home–made QCM sensor was placed inside the chamber and connected to the heater in the form of a sample to measure the deposition rate.

In the case of Se evaporator, crucible type low–temperature evaporator was used and relatively stable deposition rate can be maintained. On the other hand, in the case of the Fe evaporator, the Fe rod (2.0mm diameter, 99.995%) having a source temperature of 1200°C or higher has a sufficient deposition rate of over 1/200 Å/s under UHV conditions. However, the Fe rod gradually decreases and the deposition rate changes frequently. In this experiment, calibrating the sample just before growing the sample was tried to reduce the error. The temperature was measured using a digital pyrometer in all the experiments.

3.2 FeSe on SrTiO₃(100)

SrTiO₃(100) (STO) has a tetragonal lattice structure as well as a lattice constant of 3.905 Å, which makes it suitable for substrates of various kinds of high-temperature superconductor. In this experiment, it was tried to find out whether other kinds of superconductors could be possible in addition to the monolayer FeSe on SrTiO₃(100), which has tetragonal crystal structure, already identified as a high-temperature superconductor.

3.2.1 SrTiO₃(100) substrate preparation

Nb 0.5% doped SrTiO₃(100) (SHINKOSHA CO.) was used as a substrate for the growth of thin film FeSe. First, the STO substrate was diced to the size appropriate for the sample holder. Untreated STO substrates are semi-breakable in 15mm x 15mm x 0.5mm to 6 segments. A silicon cutter was used to deepen the gap and cut it out. The surface of these prepared STO strips can be treated smoothly through the chemical etching process. Then the STO strips were washed in the order acetone, isopropyl alcohol and distilled water, respectively, for about 5 minutes. Then, STO strips were chemically etched in a buffered oxide etcher (BOE) solution for 5 minutes to terminate the surface with TiO₂. After that, the STO strips were rinsed with distilled water and isopropyl alcohol for about 5 minutes each, and blowed off the surface with nitrogen gas. It is known that the surface of the treated STO strips is flattened at one unit cell level [29]. Then the STO strip was assembled into the sample holder. In this process, the Ti sheet was

sandwiched between the strip and the sample holder, or a Ti deposition was made on one side of the strip to make the contact resistance of the STO strip sufficiently low [30]. Normally, this process made a resistance around a few ohms. Next, the prepared sample holder was put into a growth chamber (or preparation chamber) under UHV conditions and heated to about 1200°C. If the temperature is raised too fast, the STO sample might be unevenly heated around where the thermal contact is relatively bad, which may easily be broken. The state of the sample was able to be checked through the resistance at both ends of the sample as it was heated. Through heating at high temperatures, the surface of the sample tended to make a 2x2 surface reconstruction. The FeSe was able to be grown on the thus prepared substrate. In the case of the FeSe / STO sample already grown on the substrate, it can be used repeatedly by returning to the SrTiO₃(100) strip from which the FeSe has been removed by heating again in the heater at 1200°C. Figure 3.1 shows SrTiO₃(100) observed with RHEED, LEED, STM and STS, respectively. First, the crystallization and tetragonal lattice structure of the samples were easily identified from the RHEED and LEED patterns. In addition, the surface state of the Se etched STO sample can be more reliably defined from the STS spectrum with the gap of 3.75eV and the unique modulation of the surface in the STM image.

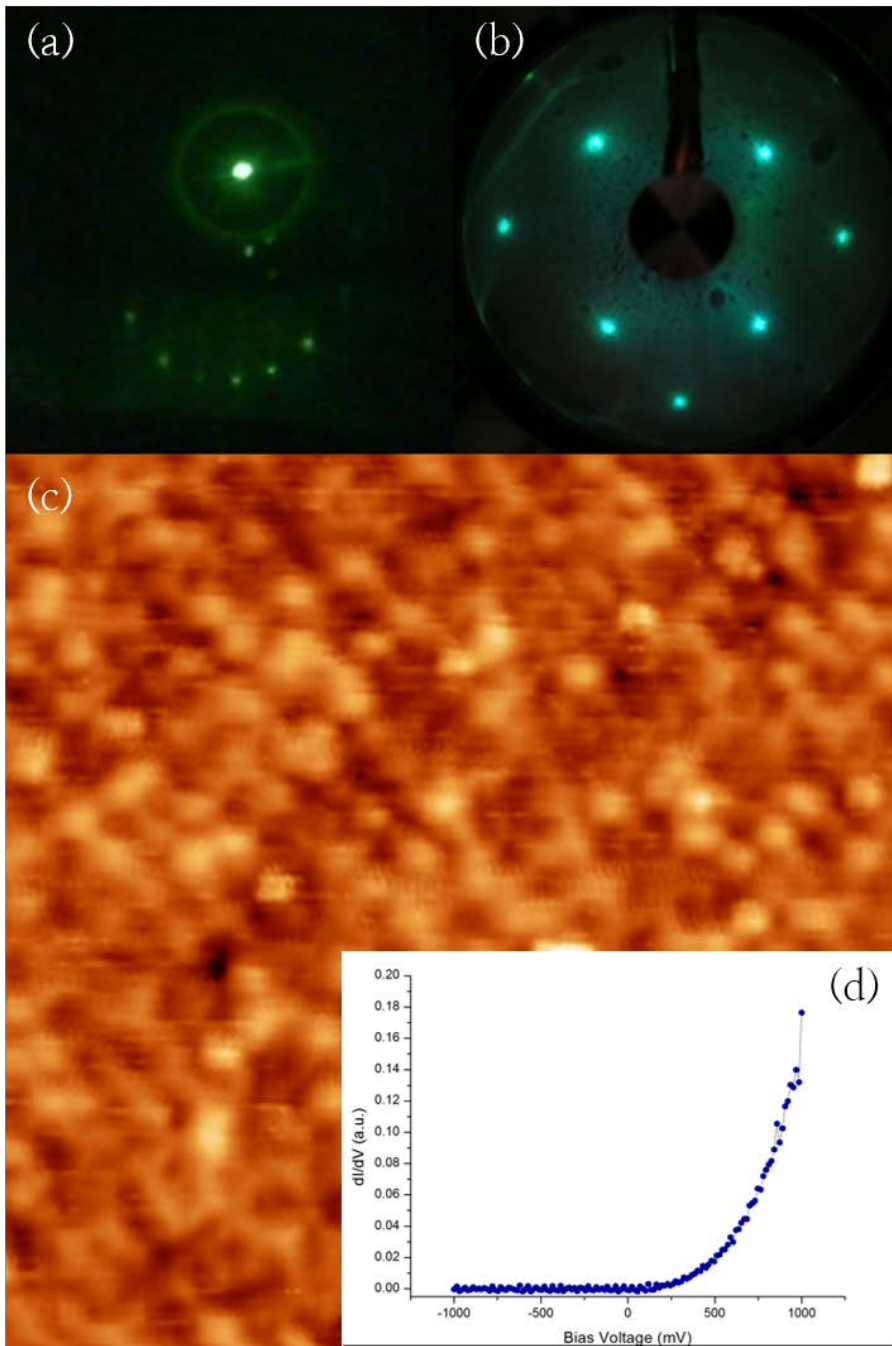


Figure 3.1: SrTiO₃(100) substrate. (a) RHEED pattern. (b) LEED pattern at 60V. (c) STM image of the surface of the Se etched SrTiO₃(100). (18nm×18nm, Reference current = 30pA, Bias = 1V) (d) Representative STS spectrum.

3.2.2 Epitaxial growth of tetragonal phases of thin film FeSe on SrTiO₃(100)

The FeSe grown in the experiment can be divided into two types, tetragonal and hexagonal depending on the lattice structure. The two most common growth modes are tetragonal structures that follow the structure of SrTiO₃(100). These tetragonal structures show various growth patterns depending on the ratio of Fe and Se deposition rate, deposition thickness, growth temperature, and surface treatment of substrate and sample. The most representative tetragonal structure of FeSe in the experiment was the epitaxial form. Based on the condition that FeSe grows as a superconducting material on the STO, most of the samples were grown at a temperature of about 450°C [31]. First, the growth rate of the samples was observed while changing the deposition rate and deposition thickness under constant temperature conditions. Figure 3.2 is the RHEED and LEED patterns of samples grown at 450°C with FeSe of 10 ML or more at a Fe:Se deposition rate of 1:15. Additional peaks for surface reconstruction was able to be seen around the tetragonal peak. Figure 3.3 and 3.4 below are investigations of the surface with STM. The samples grown under these conditions have large terrace grown epitaxially on the surface and some island formations on them. Looking at the atomic resolution image, it is reaffirmed that it has a tetragonal lattice structure. The spacing between the lattice site was about 9 Å, and it can be assumed that the thin film FeSe grown under this condition has a $\sqrt{5} \times \sqrt{5}$ surface reconstruction.

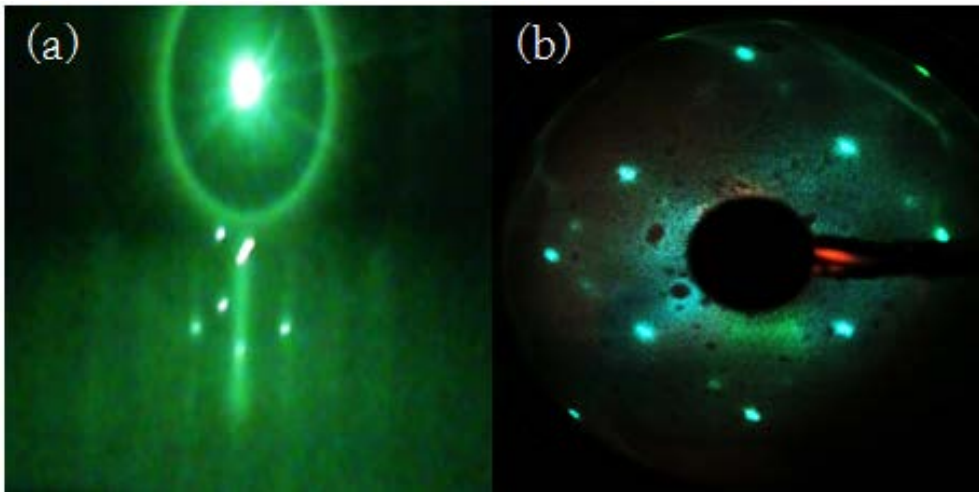


Figure 3.2: 10ML of FeSe on SrTiO₃(100) grew at 450°C. (a) RHEED pattern. (b) LEED pattern at 60V.

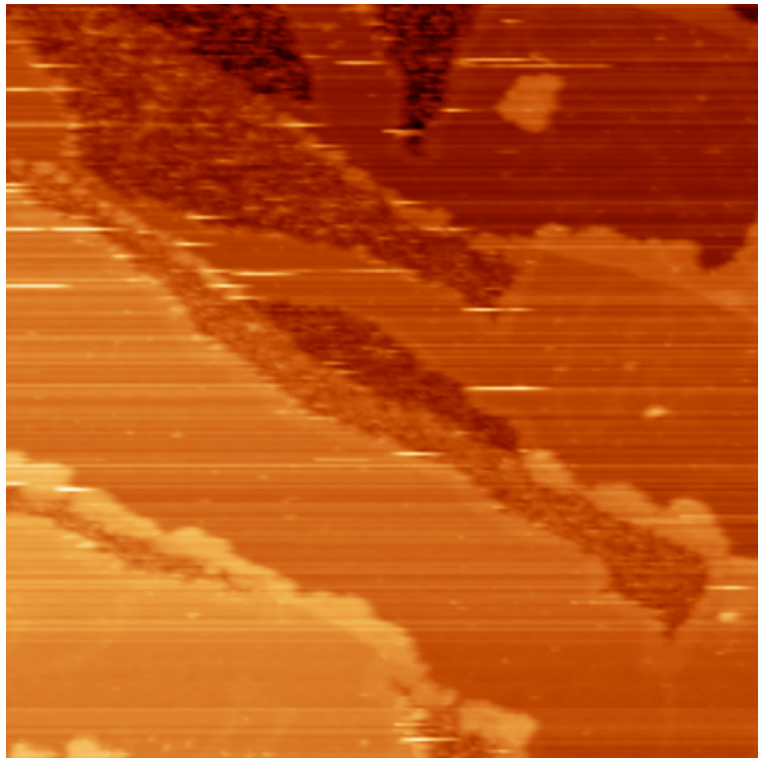


Figure 3.3: Large area STM image of 10ML of FeSe on SrTiO₃(100) grew at 450°C. (264nm×264nm, Reference current = 20pA, Bias = 2V)

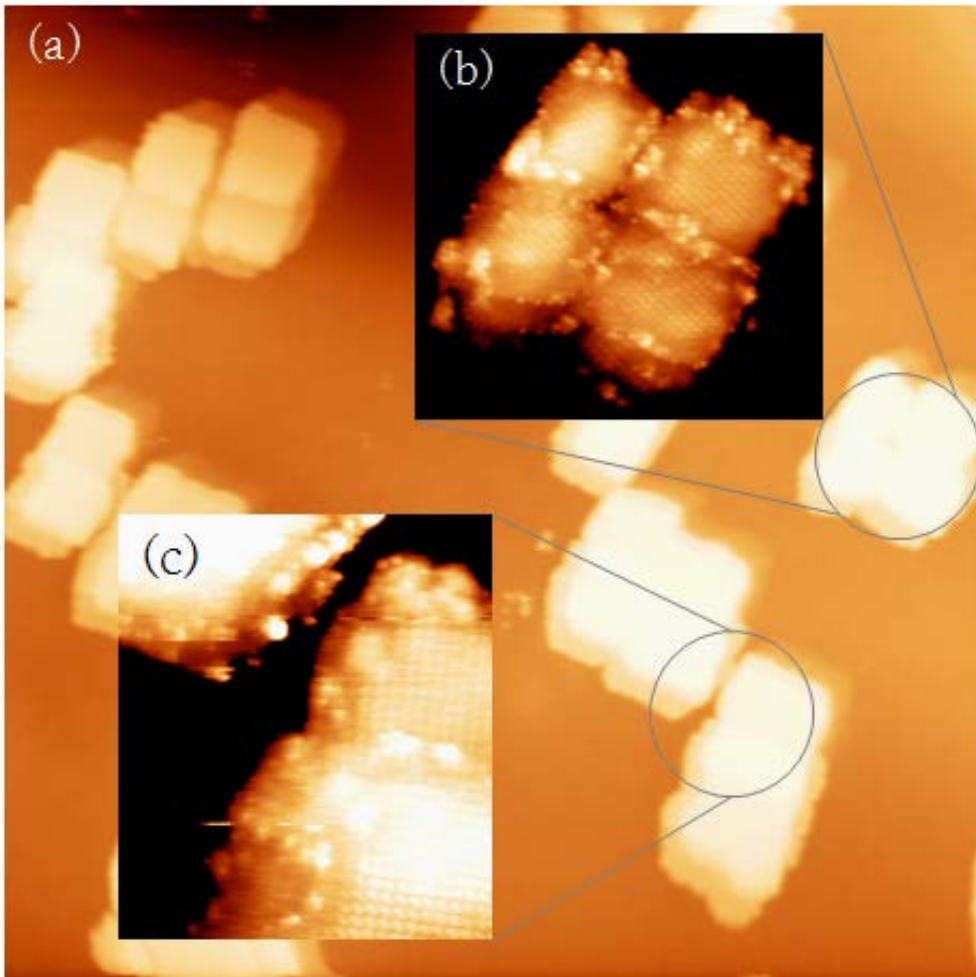


Figure 3.4: STM images of 10ML of FeSe on SrTiO₃(100) grew at 450°C. (a) 176nm×176nm, Reference current = 20pA, Bias = 2V. (b) 44nm×44nm, Reference current = 20pA, Bias = 100mV. (c) 29nm×29nm, Reference current = 50pA, Bias = 100mV. A tetragonal structure of atomic arrangement is observed in the small figures.

Figure 3.5 is the observation of a sample grown at 500°C and 600°C, respectively, only by the STM under the above conditions. The sample grown in this condition has a tetragonal structure similar to the above, and generally shows the tendency of a large terrace and a small island, which are

characteristic of a sample grown at a high temperature. It can also be seen that the surface has a modulation on a wide terrace. This is known as a naturally generated structure in which the lattice misfit between the thin film and the substrate.

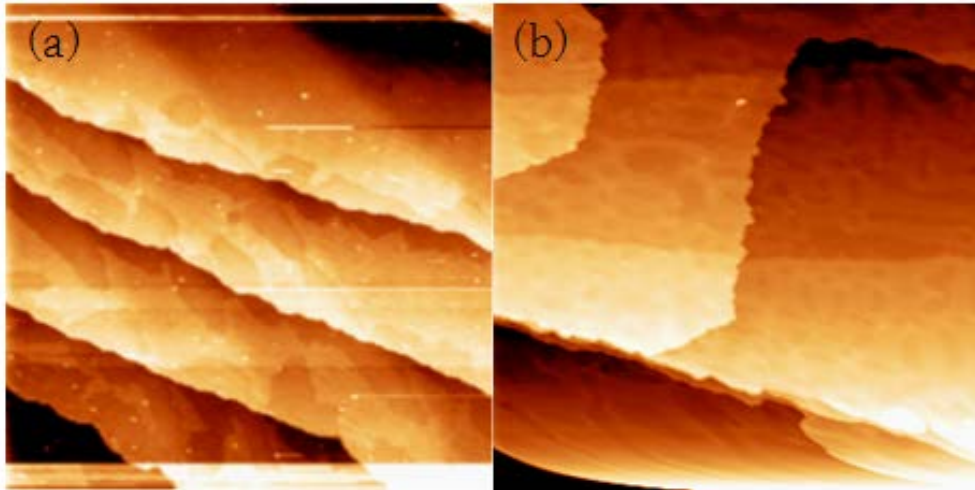


Figure 3.5: STM images of 10ML of FeSe on SrTiO₃(100) grown at various temperatures. (a) At 500°C. (270nm×270nm, Reference current = 20pA, Bias = 3V) (b) At 600°C. (270nm×270nm, Reference current = 30pA, Bias = 1V).

Next, the morphological aspect FeSe was investigated by changing the ratio of deposition flux rate of Fe:Se at 450°C and 3ML thickness condition. Sample growth conditions are as follows. First, several monolayers of Se was deposited by keeping the STO at 950°C. Thereafter, the temperature was lowered to the sample growth temperature of 450°C. Wait about 20 minutes for the temperature to stabilize, then 3ML of Fe and Se was co-deposited at the desired ratio. After the deposition was completed,

the post-annealing process was performed for about 3 hours while maintaining the temperature at 450°C.

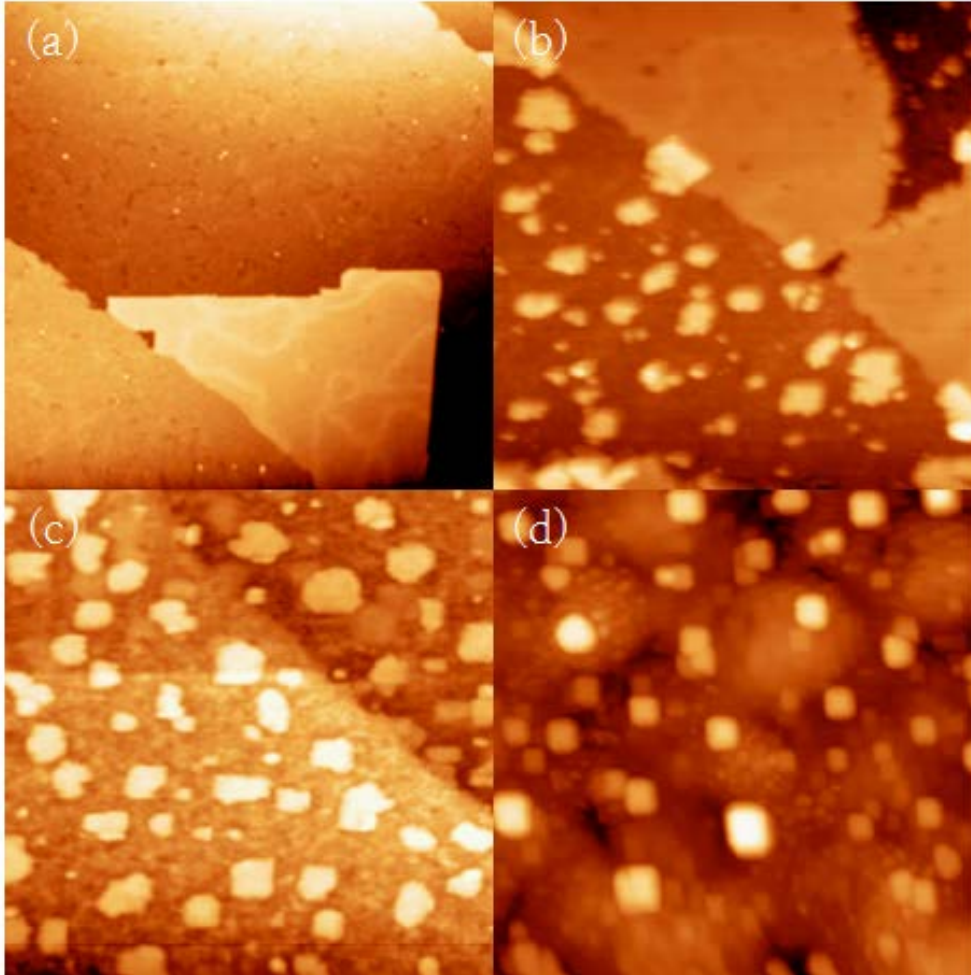


Figure 3.6: STM images of various ratios of FeSe on SrTiO₃(100) grown at 450°C. The flux ratios are (a) 1:4 (180nm×180nm). (b) 1:3 (90nm×90nm). (c) 1:0.7 (90nm×90nm). (d) 1:0.1 (90nm×90nm). All images are obtained at Reference current = 10pA, Bias = 4V.

Figure 3.6 shows the surfaces of FeSe grown on the STO with varying Fe:Se flux ratios of 1:4, 1:3, 1:0.7, and 1:0.1 respectively, were

examined at liquid nitrogen temperature of 78K. The growth pattern of the sample shows that the growth mode gradually changed from the epitaxial growth to the island growth as the ratio of Se decreased. In addition, the worm-like modulation appears again on the surface of the sample grown at a 1:4 ratio. Moreover, all structures have tetragonal lattice structure from images of atomic resolution. These can be confirmed in Figure 3.7 below.

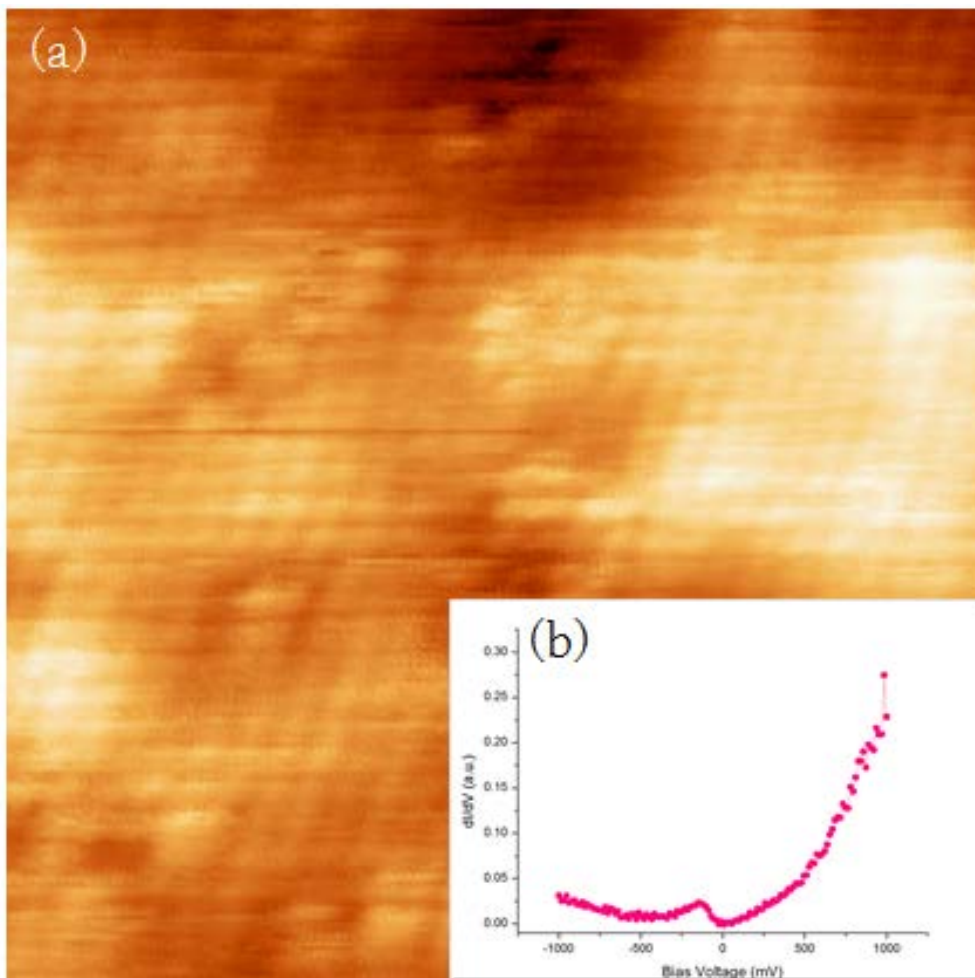


Figure 3.7: STM image of FeSe on SrTiO₃(100) grew at 450°C at atomic resolution. (a) Tetragonal arrangement of surface structure. (9nm×9nm, Reference current = 100pA, Bias = 100mV) (b) Representative STS spectrum.

3.2.3 Epitaxial growth of hexagonal phases of thin film FeSe on SrTiO₃(100)

Interestingly, under certain conditions, it was observed the growth of FeSe in the hexagonal phase rather than the normal tetragonal phase. This hexagonal lattice FeSe is known to occur only in a very narrow region of its phase diagram [32]. These conditions are not common, and hence repetitive growth is very difficult. This hexagonal phase FeSe occurred in the process of co-depositing Fe and Se at the temperature of 650°C~700°C, which is somewhat higher than the temperature at which the general tetragonal lattice is formed, and then rapidly dropping the temperature to room temperature without post annealing process. As shown in Figure 3.8 below, specific surface reconstructions were observed in the image confirmed by STM, and a large number of small triangular islands were created. Also, looking at the atomic image in Figure 3.9, it can be seen that it has a hexagonal lattice structure. It is assumed that the δ -phase FeSe, which is already known as hexagonal structure at high temperature, could not transition to the tetragonal phase while it cools rapidly. Whether the superconducting phenomenon occurs in this hexagonal phase FeSe is a further study. This type of superconductor is expected to be a new class of superconductor like p-wave superconductor, due to the symmetry of the new Fermi surfaces in the hexagonal lattice.

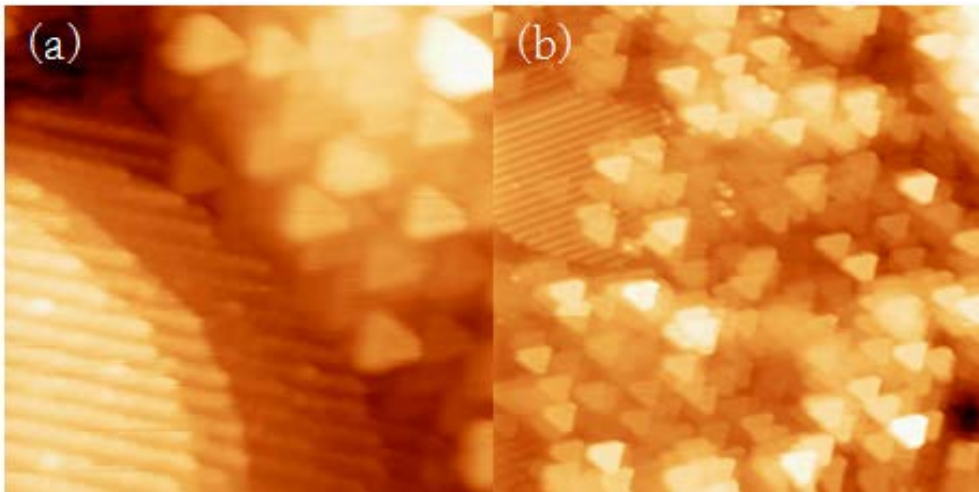


Figure 3.8: STM images of hexagonal phase FeSe on SrTiO₃(100). (a) (28nm × 28nm, Reference current = 100pA, Bias = 1V) (b) (14nm × 14nm, Reference current = 100pA, Bias = 1V)

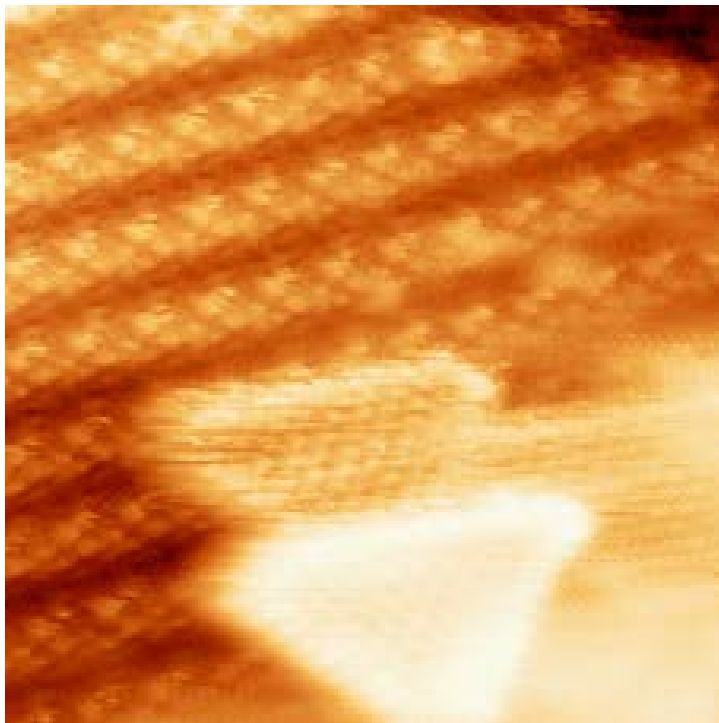


Figure 3.9: STM image of hexagonal phase FeSe on SrTiO₃(100) at atomic resolution. (14nm × 14nm, Reference current = 100pA, Bias = 1V)

3.3 FeSe on GaP(111)

GaP(111) (GaP) is a semiconductor substrate having a hexagonal structure and is not a type of substrate commonly used in high temperature superconductor growth. In this experiment, it was tried to improve the understanding of the growth conditions of hexagonal FeSe, which was occasionally observed in SrTiO₃(100) case, by using GaP substrate.

3.3.1 GaP(111) substrate preparation

2" Zn-doped GaP(111) wafer (MTI CO.) was diced to 12 mm × 12 mm × 0.5 mm according to the size of the sample holder, similar to the case of SrTiO₃(100) above. The prepared GaP strips were rinsed in acetone, isopropyl alcohol and distilled water for 2 minutes each. The GaP strip was then proceeded to chemical etching to remove impurities and planarize the surface [33]. As in the case of STO, chemical etching was performed using an acid. The chemical etching was performed using 12% hydrochloric acid solution, aqua regia and BOE solution. The GaP surface etched for 10 seconds in these solutions showed no significant difference between the solutions.

It was notable that since Zn-doped GaP was a semiconducting material, and the approach of STM tip was very difficult in normal cases. This phenomenon was thought to be due to the surface resistance being very large, which was about several hundreds of megaohms. To reduce the surface resistance of the GaP, Pd deposition was applied to both ends of the

GaP strip to convert the metal–semiconductor junction between the sample holder and the GaP strip into ohmic contact. Figure 3.10 (a) below shows a Pd deposited GaP(111) strip. After the Pd deposition was made, the surface resistance became to several hundreds of ohms, and a certain Ohmic contact was generated. Another reason for the difficulty of STM tip approach was that a p–n junction was created at the surface of GaP strip. The GaP used in the experiment was a Zn–doped p–type semiconductor material. It was thought that the exposed part of GaP strip for the STM scanning of the sample was contaminated inside the chamber and made such a p–n junction by n–type doping at the top of the surface. This was improved by contacting the sample holder with the exposed part of the GaP strip with a thin Au wire. Another way to solve this problem is using other type of doped wafers, avoiding making p–n junctions. The wafer that can be used here is S–doped GaP(111).

The prepared GaP strip was cleaned by repeating several times of ion bombardment and annealing using Ne and Ar gas in a UHV chamber. Note that the pressure inside the chamber should not be too high because the GaP is outgassing more than the STO during the cleaning process. In order to obtain a clean GaP(111) surface again, it was sufficient to clean FeSe/GaP by the means of ion bombardment and annealing several times. Figure 3.10 (b) below is the LEED pattern of cleaned GaP(111). As expected, it has a hexagonal pattern. It can be seen that there are surface reconstructions other than 1x1 in GaP(111) in the shape of small peaks around each main peak.

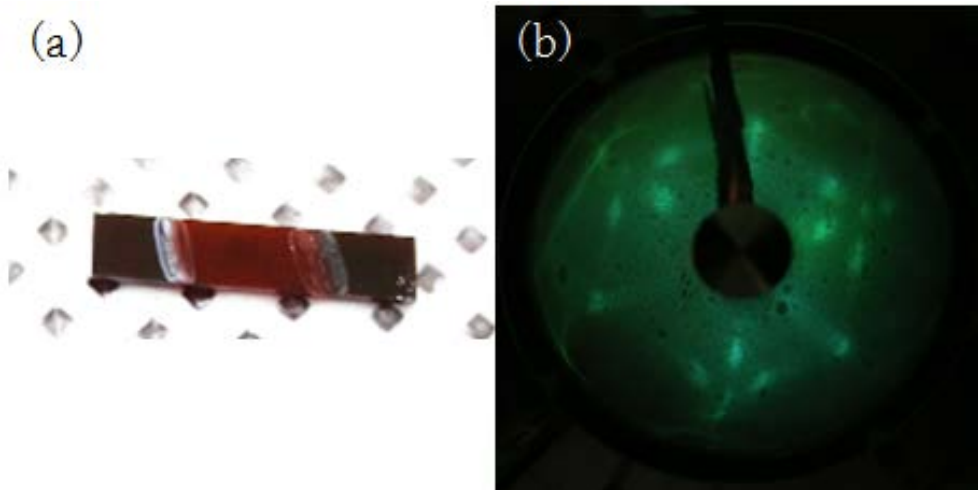


Figure 3.10: GaP(111) substrate. (a) A strip of GaP(111) wafer after Pd deposition at the both ends of it. (b) LEED pattern at 60V.

The following Figure 3.11 (a) and (b) are images of the surface of GaP(111) observed with STM at liquid nitrogen temperature 78K. Hexagonal and truncated triangular shaped terraces were stacked several times, representing the characteristic of a hexagonal lattice. The size of one terrace was more than 10nmx10nm, which was considered to be a sufficient substrate for epitaxial growth. The electronic structure of the GaP(111) surface was also studied with STS. In Figure 3.11 (c), the clean surface of GaP(111) showed typical semiconductor properties when viewed through STS, and the gap of 1.8eV was slightly smaller than the known gap of 2.26eV.

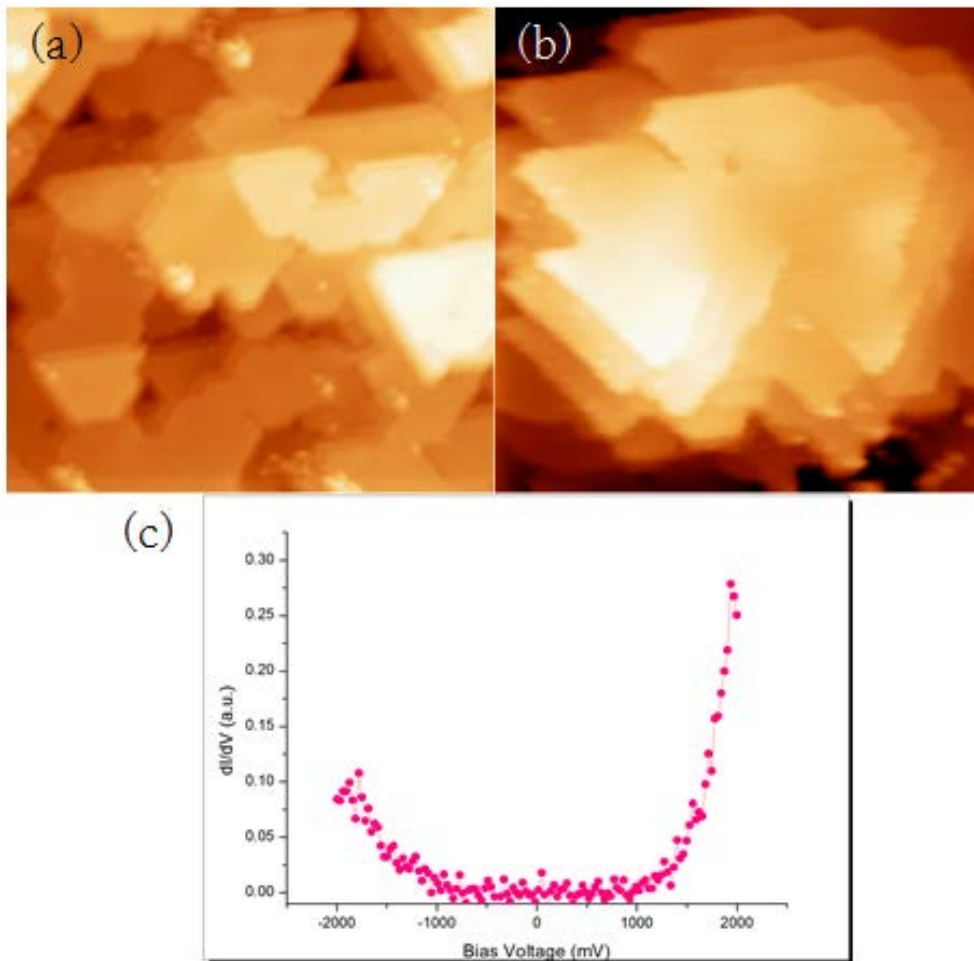


Figure 3.11: STM images of GaP(111) substrate. (a) $14\text{nm} \times 14\text{nm}$, Reference current = 100pA, Bias = 1V. (b) $14\text{nm} \times 14\text{nm}$, Reference current = 100pA, Bias = 1V. (c) Representative STS spectrum.

3.3.2 Growth of thin film FeSe on GaP(111)

The growth recipe of FeSe on GaP (111) was as follows. First, a clean GaP(111) sample was loaded into a heater in a growth chamber and heated to about 350°C . At the same time as the heating started, the Se evaporator also started preheating. The shutter of the preheated Se evaporator was opened for 30 minutes to deposit Se on the GaP(111)

surface for a coverage of about 1ML. This process was intended to make GaSe buffer surface at the top of the substrates. After that, close the shutter of the evaporator and heat it for 5 minutes with the deposition stopped. Then, the Fe evaporator and the shutter of the Se evaporator were simultaneously opened to grow the FeSe sample to a thickness of about 3ML. The flux ratio of Fe: Se was about 1:10, which is the epitaxial growth condition on the STO substrate. After co-deposition, the temperature was lowered to about 350°C and the sample was post-annealed for about 3 hours.

Figure 3.12 (a) is the LEED pattern of this Se etched GaP(111) surface. Compared with the LEED pattern of Cleaned GaP(111), it is characteristic that the surrounding reconstruction peak disappeared and only the hexagonal pattern remained. Figure 3.12(b) is the LEED pattern of FeSe on GaP (111) after growth, which is very similar to the that of Se etched GaP(111). As described above, this is probably due to the formation of a GaSe buffer layer which has a lattice structure similar to that of FeSe during the Se etching process. The following Figure 3.13 is the surface of FeSe on GaP examined at liquid nitrogen temperature 78K. It can be seen that the shape of the surface made the growth of a small triangular island. The height of the triangular island is approximately 6Å. The electronic structure of FeSe on GaP studied using STS showed that it has metallic properties near zero bias. In Figure 3.14, it can be shown that the FeSe on GaP(111) has a metallic feature at the zero bias. However, it is failed to look at these electronic properties at liquid helium temperature. At liquid helium temperatures, the tip and the sample made a diode-like junction,

presumably because the contact of the Au wire made to lower the surface resistance broken due to thermal effects at low temperatures near 8K.

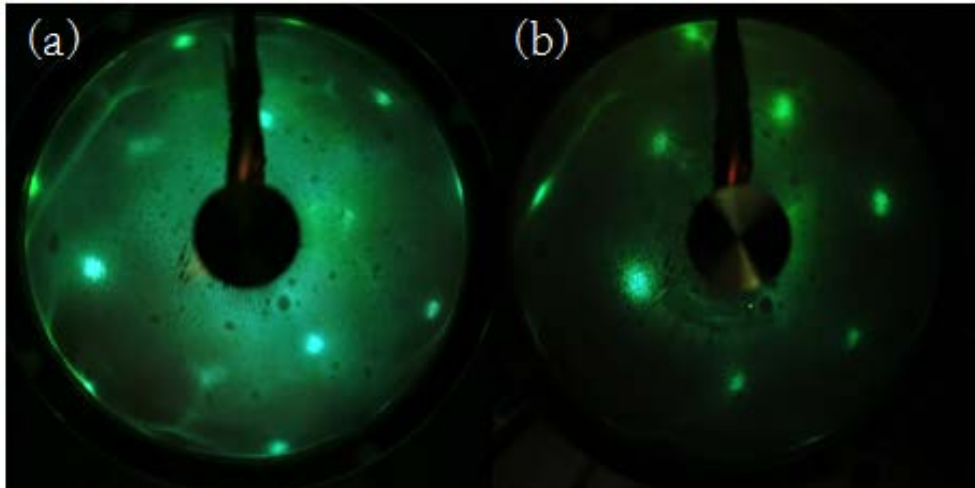


Figure 3.12: LEED patterns at 60V of (a) Se etched GaP(111) and (b) FeSe on GaP (111).

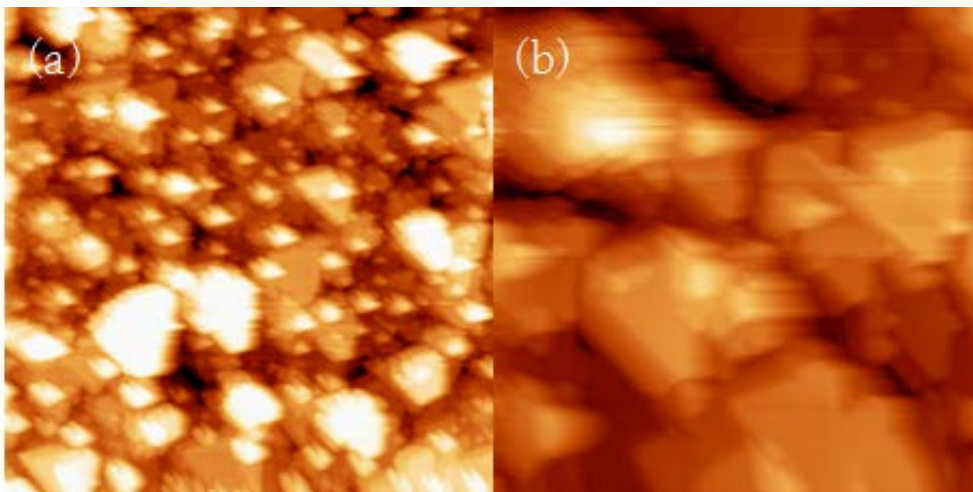


Figure 3.13: STM images of FeSe on GaP(111). (a) $290\text{nm} \times 290\text{nm}$, Reference current = 10pA, Bias = -4V . (b) $98\text{nm} \times 98\text{nm}$, Reference current = 10pA, Bias = -3V .

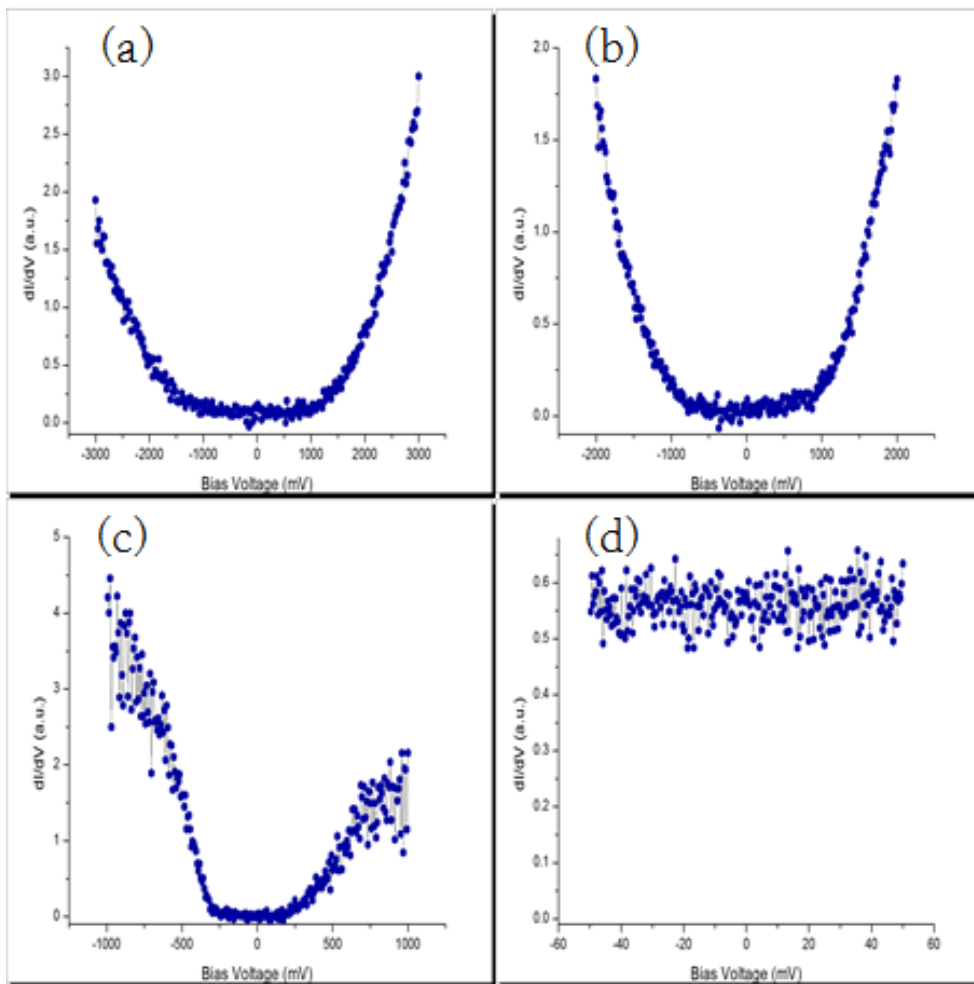


Figure 3.14: STS spectra of FeSe on GaP(111) at various bias voltages. (a) Bias = 3V. (b) Bias = 2V. (b) Bias = 1V. (b) Bias = 50mV. Note that the dI/dV spectra at zero bias is not zero value.

Bibliography

- [1] H. K. Onnes, The resistance of pure mercury at helium temperatures, *Comm. Phys. Lab. Univ. Leiden*, Vol. 12, 120 (1911).
- [2] F. London and H. London, The electromagnetic equations of the supraconductor, *Proc. Roy. Soc. (London)*, A149, 71 (1935).
- [3] V. L. Ginzburg and L. D. Landau, *Zh. Eksp. Teor. Fiz.* 20, 1064 (1950).
- [4] J. Bardeen, L. N. Cooper, and J. R. Schrieffer, Microscopic theory of superconductivity, *Phys. Rev.* 106, 162 (1957).
- [5] J. Bardeen, L. N. Cooper, and J. R. Schrieffer, Theory of superconductivity, *Phys. Rev.* 108 1175 (1957).
- [6] L. N. Cooper, Bound electron pairs in a degenerate Fermi gas, *Phys. Rev.* 104, 1189 (1956).
- [7] N. N. Bogoliubov, *Nuovo Cimento* 7, 794 (1958).
- [8] J. G. Bednorz and K. A. Müller, Possible high T_c superconductivity in the Ba-La-Cu-O system, *Z. Phys. B.* 64, 189 (1986).
- [9] M. K. Wu et al., Superconductivity at 93K in a new mixed-phase Y-Ba-Cu-O compound system at ambient pressure, *Phys. Rev. Lett.* 58, 908 (1987).
- [10] H. Maeda et al., A new high- T_c oxide superconductor without a rare earth element, *Jpn. J. Appl. Phys.* 27, L209 (1988).
- [11] Z. Z. Sheng and A. M. Hermann, Bulk superconductivity at 120K in the Tl-Ca/Ba-Cu-O system, *Nature* 332, 138 (1988).
- [12] H. Hosono et al., Iron-based layered superconductor $\text{La}[\text{O}_{1-x}\text{F}_x]\text{FeAs}$ ($x=0.05-0.12$) with $T_c=26\text{K}$, *J. Am. Chem. Soc.* 130 (11), pp 3296-3297 (2008).

- [13] H. Hosono and K. Kuroki, Iron-based superconductors: current status of materials and pairing mechanism, *Physica C*, 514, 399 (2015).
- [14] J. Paglione and R. L. Greene, High-temperature superconductivity in iron-based materials, *Nature phys.* 6, 645–658 (2010).
- [15] K. Momma and F. Izumi, VESTA: a three-dimensional visualization system for electronic and structural analysis, *J. Appl. Cryst.* 41, 653–658 (2008).
- [16] H. Hosono et al., Exploration of new superconductors and functional materials, and fabrication of superconducting tapes and wires of iron pnictides, *Sci. Technol. Adv. Mater.* 16, 033503 (2015).
- [17] S. B. Zhang et al., Crystal growth and superconductivity of FeSe_x, *Supercond. Sci. Technol.* 22, 015020 (2009).
- [18] Q. Fan et al., Plain s-wave superconductivity in single-layer FeSe on SrTiO₃ probed by scanning tunneling microscopy, *Nature Phys.* 11, 946–952 (2015).
- [19] S. He et al., Phase diagram and electronic indication of high-temperature superconductivity at 65K in single-layer FeSe films, *Nature Mat.* 12, 605–610 (2013).
- [20] J.-F. Ge et al., Superconductivity above 100K in single-layer FeSe films on doped SrTiO₃, *Nature Mat.* 14, 285–289 (2015).
- [21] Q. Wang et al., Strong interplay between stripe spin fluctuations, nematicity and superconductivity in FeSe, *Nature Mat.* 15, 159–163 (2016).
- [22] X. Liu et al., Electronic structure and superconductivity of FeSe-related superconductors, *J. Phys.: Condens. Matter* 27, 183201 (2015).
- [23] Z. F. Wang et al., Topological edge states in a high-temperature

- superconductor FeSe/SrTiO₃(001) film, *Nature Mat.* 15, 968–973 (2016).
- [24] G. Binnig et al., Surface studies by scanning tunneling microscopy, *Phys. Rev. Lett.* 49, 57 (1982).
- [25] J. Bardeen, Tunneling from a many-particle point of view, *Phys. Rev. Lett.* 6, 57 (1961).
- [26] C. J. Chen, Introduction to Scanning Tunneling Microscopy, OUP Oxford (2008).
- [27] A. Y. Cho and J. R. Arthur, Molecular beam epitaxy, *Prog. Solid State Chem.* 10, 157–192 (1975).
- [28] J.-F. Jia et al., STM and MBE: one of the best combinations, *J. Phys. D: Appl. Phys.* 44, 464007 (2011).
- [29] M. Kawasaki et al., Atomic control of the SrTiO₃ crystal surface, *Science* 266, 1540 (1994).
- [30] D. J. Jefferies, High-field Ohmic contacts to semiconducting SrTiO₃ single crystals, *J. Appl. Phys.* 47, 778 (1976).
- [31] Q.-Y. Wang et al., Interface-induced high-temperature superconductivity in single unit-cell FeSe films on SrTiO₃, *Chinese Phys. Lett.* 29, 037402 (2012).
- [32] H. Okamoto, The FeSe (iron-selenium) system, *J. Phase Equilib.* 12, 383 (1991).
- [33] K. Hattori et al., GaP(111) reconstructed surface studied with STM and LEED, *Surf. Sci.* 525, 57 (2003).

Appendix

Appendix A

STM Tip Fabrication by Electrochemical Etching and Focused Ion Beam (FIB)

The STM tips used in the experiments are made of metallic materials. These STM tips use a variety of metals to suit the purpose of the experiment. For example, to make superconductor–vacuum–superconductor (SVS) junctions, a tip with superconducting properties such as niobium is used, and a tip with hard physical properties such as tungsten is used to define mechanically well. The tips used in this experiment are of two types, tungsten and iridium. For the electrochemical etching process, use a tungsten tip for KOH solution and an iridium tip for CaCl_2 solution. Through this process, the refined tip has a radius of curvature of about 1 micrometer at its apex. Typically, the tungsten tip is combined with the STM head after several repetitions of heating and flashing by the method of electron bombardment in the tip heater after this electrochemical etching process. Focused Ion Beam (FIB) is used to obtain a tip apex that is sharper than the iridium tip. Figure A.1 shows the iridium tip obtained at several magnifications using a scanning electron microscope (SEM). The iridium tip obtained by electrochemical etching can be made to have a radius of curvature of 30 nm or less at its apex by using Gallium FIB in three

Appendix B

Epitaxial Growth of Monolayer GeSe on Ge(111)

Experiments on the growth of thin film GeSe on Ge(111) substrates were carried out prior to the experiments on the growth of thin film FeSe on SrTiO₃(100) and GaP(111) substrates in this thesis. The growth of these two-dimensional semiconductor materials is essential for studying functional interfaces for other purposes in addition to high temperature thin film superconductors. Since GeSe is a IV-VI semiconductor material with strong anisotropy, it attracts much attention in the development of optoelectronics devices. Here, the system used for the growth of the thin film GeSe is a variable low temperature STM-MBE combined system. The growth of the sample was performed on a Ge(111) substrate using a crucible type Se evaporator at a UHV condition pressure of 2.0×10^{-10} torr or less. The samples were observed at 78K under liquid nitrogen condition and STM and STS at low temperature of 8.2K under liquid helium condition. Figure B.1 below shows the surface of monolayer GeSe observed with STM. After the growth, a large area of monolayer GeSe can be obtained by annealing at 190°C. Figure B.2 shows the surface of the sample again at atomic-level resolution. In this way, we can observe a surface similar to the orthorhombic structure of known GeSe crystal structure. The point that is unique in this part is that its lattice constant is much larger in one direction than the original bulk crystal structure. Whether this is a precisely stretched structure or a structure that emerges through other forms of surface

reconstruction seems to require further investigation. Figure B.3 shows the surface obtained by increasing the deposition time while maintaining a constant deposition rate of Se. In terms of surface morphology, it seems that epitaxial growth continues even when the monolayers grow from 1 monolayer, 3 monolayers to 5 monolayers. A particularly interesting property in this system is the heterojunction between Ge(111) substrate and monolayer of GeSe grown on top of the substrate. Figure B.4 shows that this semiconductor–semiconductor interfacial band bending occurs using line STS. Finally, Figure B.5 shows the measurement of bosonic mode using Inelastic Scanning Tunneling Spectroscopy (IETS). In general, these IETS are not easy to measure because of their small signal amplitude. It can be seen that bosonic modes assumed to be phonons appear at 9meV, 22meV and 40meV.



Figure B.1: STM image of monolayer GeSe on Ge(111). (50nm \times 50nm, Reference current = 30pA, Bias = -2V)

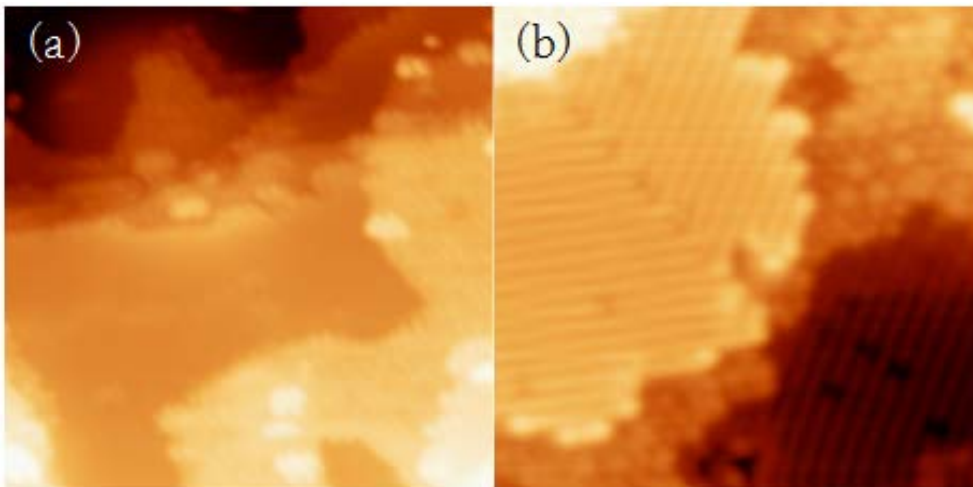


Figure B.2: STM images of multilayer GeSe on Ge(111). (a) 3~4ML GeSe. (50nm \times 50nm, Reference current = 100pA, Bias = 1V) (b) 4~5ML GeSe. (50nm \times 50nm, Reference current = 100pA, Bias = 1V)

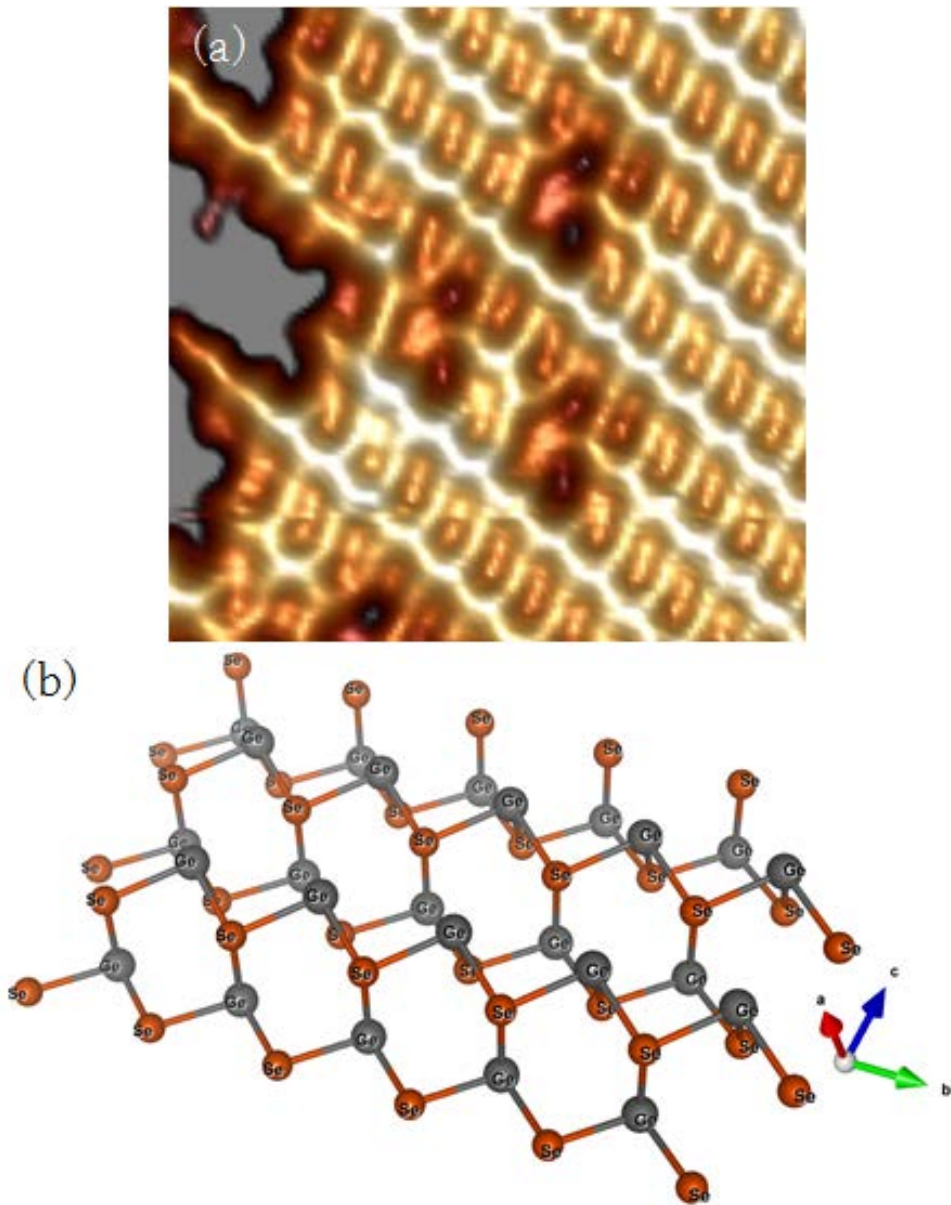


Figure B.3: Crystal structure of monolayer GeSe on Ge(111). (a) STM image of monolayer GeSe on Ge(111) at atomic resolution. (5nm×5nm, Reference current = 100pA, Bias = 1V) (b) Orthorhombic (symmetry: Pnma) lattice structure of GeSe.

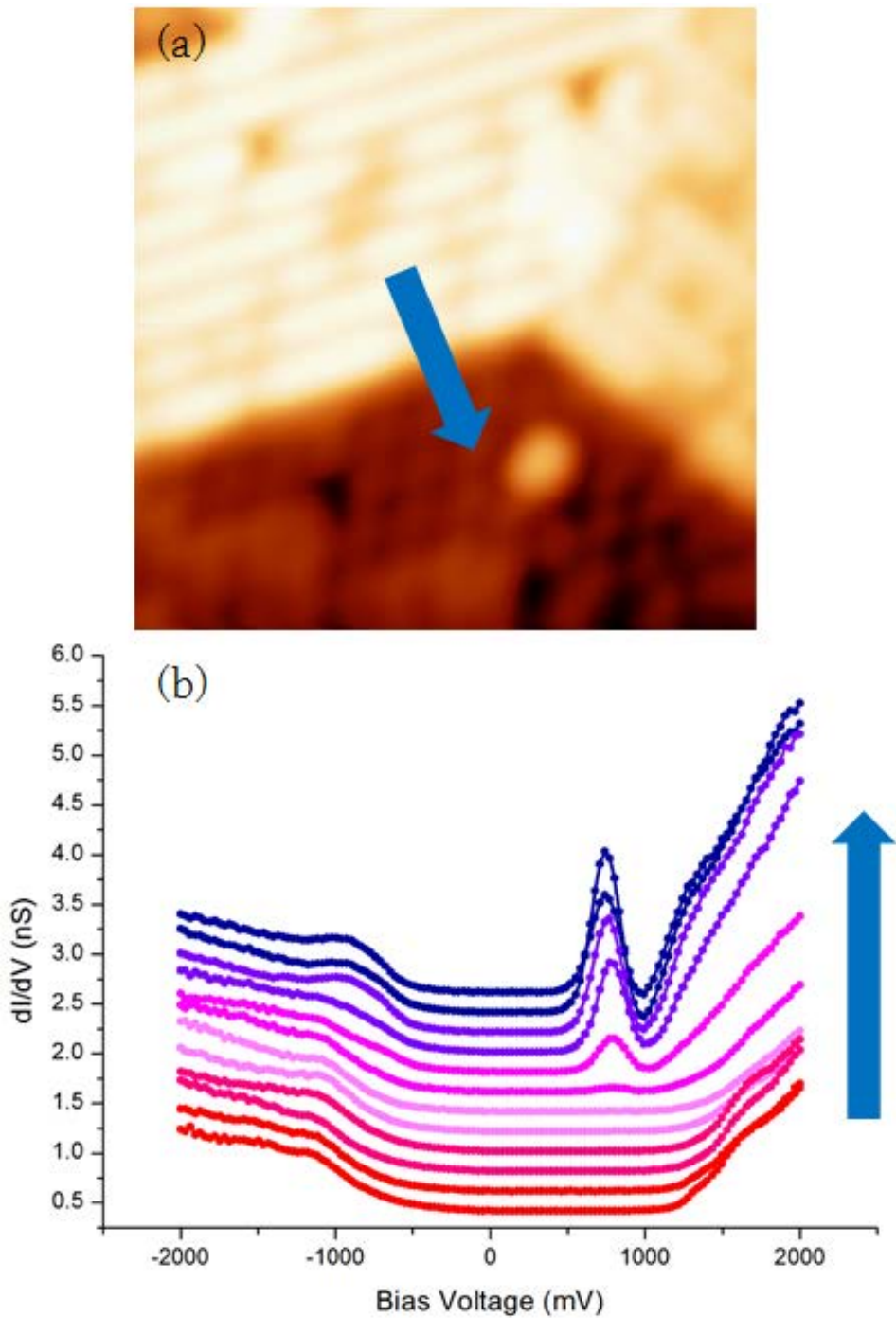


Figure B.4: Heterojunction between monolayer GeSe on Ge(111) and Ge(111) substrate. (a) STM image of the heterojunction. ($5\text{nm} \times 5\text{nm}$, Reference current = 500pA , Bias = 1V) (b) Orthorhombic (symmetry: $Pnma$) lattice structure of GeSe.

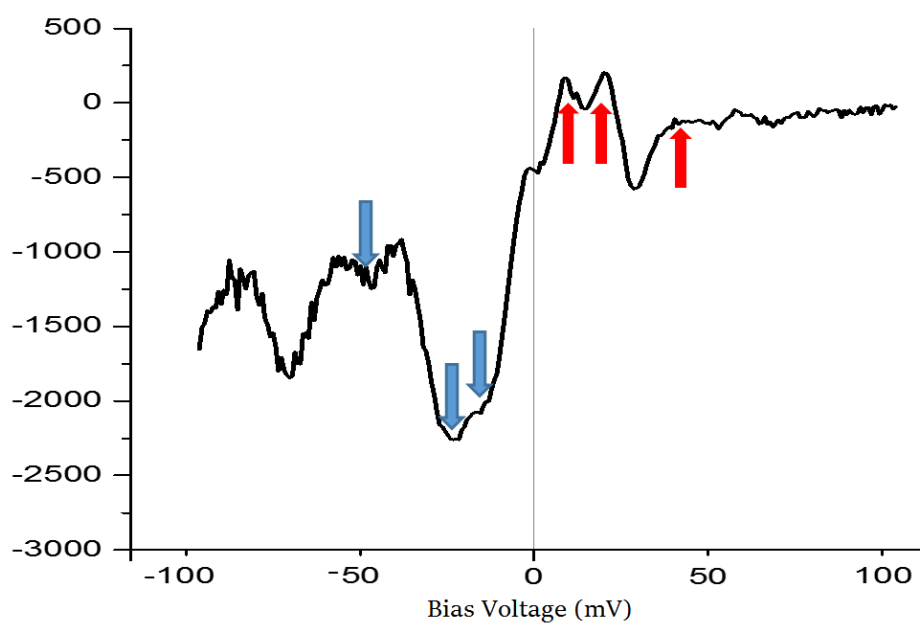


Figure B.5: IETS spectra of monolayer GeSe on Ge(111).

국 문 초 록

고온 초전도현상은 응집물질물리학에서 가장 중요한 연구분야 중 하나이다. 특히 철기반 고온 초전도체는 기존의 초전도체를 구성하고 있던 BCS 초전도체나 구리기반 초전도체와는 완전히 다른 페르미 레벨의 대칭성을 가지고 있기 때문에 그 초전도 현상의 메커니즘을 설명하기 위한 새로운 물리학을 필요로 하고 있다. 그 중에서도 철 칼코겐 화합물인 FeSe는 상대적으로 간단한 구조를 가지면서 매우 높은 초전도 상전이 온도를 가질 수 있는 물질로 연구 가치가 높다. 이 논문은 이러한 FeSe의 SrTiO₃(100)과 GaP(111) 기판 위에서의 얇은 박막 형태의 성장을 다루고 있다. 이 실험에서 FeSe 시료는 Fe와 Se를 수정 진동자 계측기(QCM)로 조정된 분자선 에피택시(MBE)를 이용하여 기판 위에 성장되었다. 성장 중인 시료의 결정성은 저에너지 전자 회절(LEED)과 고에너지 반사 전자 회절(RHEED)을 통해 확인되었다. 여러 가지 조건에서 성장된 시료는 초고진공 챔버 내부에서 오염되지 않은 상태로 주사형 터널링 현미경(STM)과 주사형 터널링 분광법(STS)을 통해 액체질소와 액체헬륨의 저온에서 그 표면과 전자구조가 조사되었다. 조사된 시료는 SrTiO₃(100) 기판 위에서 정방정계 구조와 GaP(111) 기판 위에서 육방정계 구조를 나타내었다. 이러한 구조들의 다양한 원자적 수준의 표면 재구성 역시 확인되었다.

주요어: 철기반 초전도체, 철 칼코겐 화합물, 박막, 분자선 에피택시, 주사형 터널링 현미경

학 번: 2015-20339